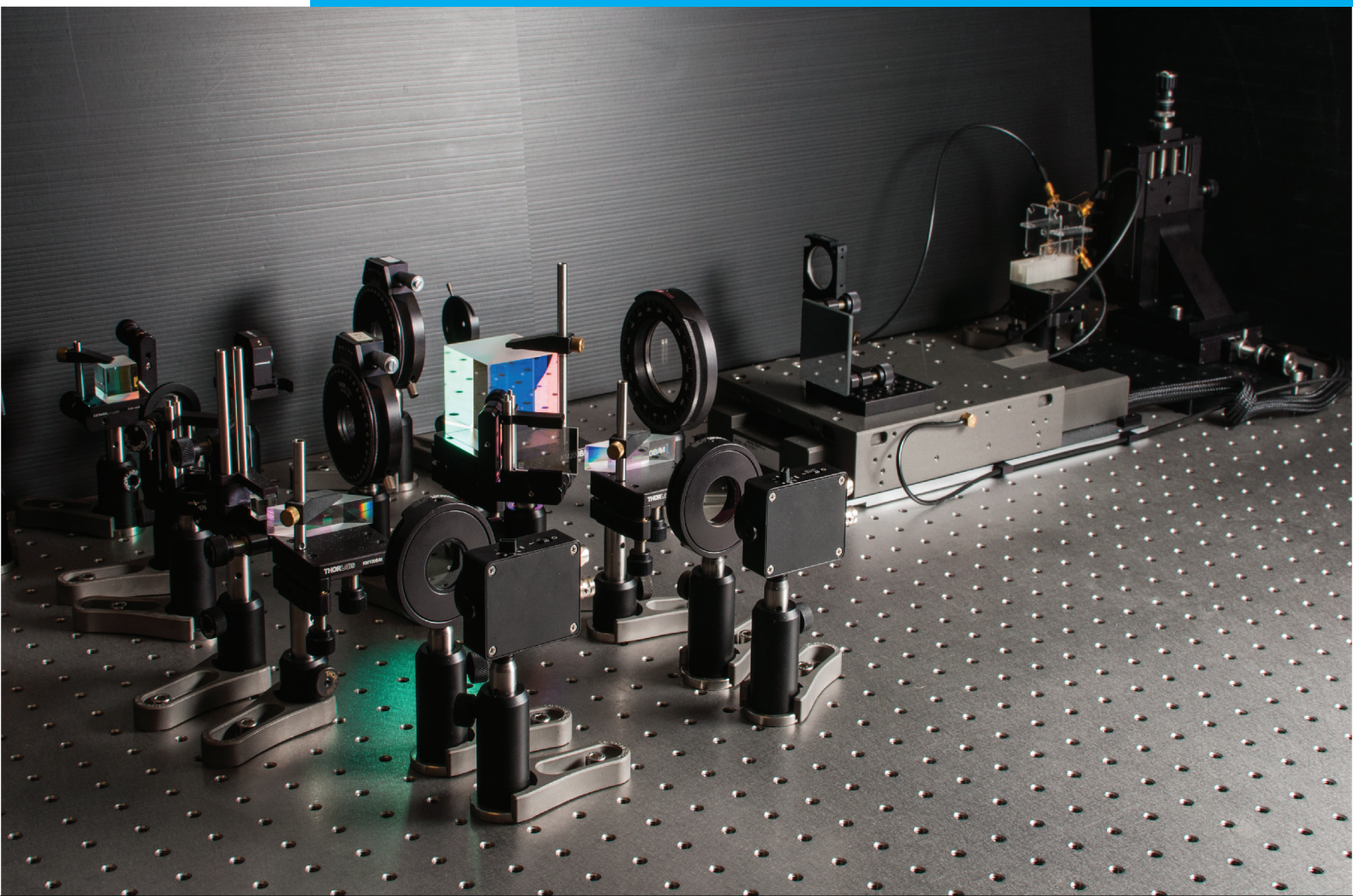


## Department of Precision and Microsystems Engineering

### Optical frequency shifting using (electro-optic) rotating wave-plates and its application in heterodyne displacement interferometry

R.T. van der Niet

Report no. : MSD 2015.017  
Coach : dr. ir. A.J.H. Meskers  
Professor : Prof. dr. ir J.L. Herder  
Specialisation : Mechatronic System Design  
Type of report : Master Thesis  
Date : 26-08-2015





OPTICAL FREQUENCY SHIFTING USING (ELECTRO-OPTIC)  
ROTATING WAVE-PLATES AND ITS APPLICATION IN HETERODYNE  
DISPLACEMENT INTERFEROMETRY

by

**R.T. van der Niet**

in partial fulfillment of the requirements for the degree of

**Master of Science**  
in Mechanical Engineering

at the Delft University of Technology,  
to be defended publicly on Wednesday September 9, 2015 at 12:45.

Supervisor:	dr. ir. A. J. H. Meskers,	TNO/TU Delft
Thesis committee:	Prof. dr. ir. J. L. Herder,	TU Delft
	ir. J. W. Spronck,	TU Delft
	dr. ir. W. J. Venstra,	TU Delft



# PREFACE

## REPORT STRUCTURE

This report is part of the final examination for the MSc. Precision & Microsystems Engineering: Mechatronic System Design. The main body of this report consists of two chapters, readable as separate documents. The first chapter contains the primary graduation document; a scientific paper written for publication purposes. This paper incorporates an introduction to the topic, as well as all the relevant results that were produced during the research over the past 12 months.

In addition, a second document has been written, hereafter referred to as Appendix. The Appendix includes a practical guide for the most important equipment that has been utilized during this research. This document is solely written for students, researchers and staff that will either continue this research, or use the same devices for a different purpose. It contains tips & tricks for the most critical steps that have to be taken in order to use the devices within a relatively short amount of time.

## ACKNOWLEDGEMENTS

Hereby I would like to thank all the people that have been, in one or the other way, involved in my last year of study at the TU Delft. That includes all the students, researchers and technical-staff within the Mechatronic System Design group; Johan, Oscar, Foppe, Ruijun, Paul, Gihin, Charlie, Rens, Arjan S., Haris, Martijn, Stefan, Bart, Erik, Floris, Pjotr, Ruud H., Lukas, Rob, Patrick and Harry. Thank you for all the things that I have learned from you during the various 'Jo'-meetings and coffee-breaks. But most of all, I want to thank you for the incredible time I had this last year.

Jo, I would like to thank you for your advice and guidance throughout this research. Not only have I learned a lot from you with respect to the scientific part, I am also very grateful for many other things I learned this year. You taught me to always be critical, to ask questions and to sometimes leave the beaten track, even though that might mean breaking the rules. I am convinced this aforementioned mentality will help me throughout the rest of my career, for which I am very thankful.

Arjan, I want to thank you for the excellent guidance you gave me during the research, I could not have wished for a better supervisor. Apart from that, you are above all a very smart, reliable and kind person.

Furthermore I would like to thank Warner Venstra for very useful feedback with respect to the performed research.

Sten, Jaap & Merlijn, I would like to thank you for everything I have learned during the research performed in the Honours Programme project. Sten, thank you for all the fun and interesting discussions we had this year. Moreover, I would like to thank you for being a great friend. Jaap, thank you for your numerous attempts to make me switch from MATLAB to Python, which eventually succeeded and for which I am very grateful. (Yes, all the readers should switch too!)

At last, but not least, I would like to thank my parents and sister for their endless support throughout the years.

*R.T. van der Niet  
Delft, August 2015*



**1**

**SCIENTIFIC PAPER**



# Optical frequency shifting using (electro-optic) rotating wave-plates and its application in heterodyne displacement interferometry

Ruud T. van der Niet,<sup>1</sup> Arjan J.H. Meskers,<sup>1,2</sup> and Jo W. Spronck<sup>1</sup>

<sup>1</sup>*Delft University of Technology, Department of Precision and Microsystems Engineering, Mekelweg 2, 2628 CD Delft, The Netherlands*

<sup>2</sup>*TNO Technical Sciences, Department of Optomechatronics, Stieltjesweg 1, 2628 CK Delft, The Netherlands*

(Dated: August 26, 2015)

The generation of a split-frequency is inherent to heterodyne displacement interferometry. Currently this split-frequency is predominantly generated by either acousto-optic modulators (AOM), Zeeman-lasers (ZL), or a combination. Both techniques have their drawbacks, e.g. AOM have a limited bandwidth and are optically inefficient due to a loss of optical power in various unused diffraction orders. Whereas the optical output power of a Zeeman-laser decreases rapidly as the split frequency is increased. This publication presents a third method to generate split-frequencies for heterodyne displacement interferometry, making use of an electro-optic rotating quarter wave-plate. Using this technique, the split-frequency is tunable, optical power is preserved, and the technique has potential to generate split-frequencies of several MHz. Moreover, this publication contains a complete review of frequency-modulation using rotating mechanical- and electro-optic wave-plates. The rotating electro-optic quarter wave-plate is implemented in a heterodyne displacement interferometer and compared to state-of-the-art split-frequency generation techniques in terms of periodic non-linearity (PNL). Experimental results showed a first order PNL of 2.7nm obtained with the presented electro-optic split-frequency generator, in contrast to 1.6nm and 0.18nm for the ZL and AOM respectively.

## I. Introduction

Throughout the last decades, heterodyne laser interferometry has become ever more important across the field of metrology. The measurement technique is applied in various fields of research, ranging from measuring stage displacement in high-precision metrology<sup>1,2</sup>, detecting gravitational waves in the LIGO<sup>3</sup> and LISA projects<sup>4,5</sup>, to measuring the orbital angular momentum of a single photon.<sup>6</sup> Additionally, the technique is often used to calibrate several types of capacitive- and inductive sensors, exploiting its non-contact measurement capability, high resolution (sub-nm) and large dynamic range.

Inherent to heterodyne interferometry is the generation of a split frequency. Such a split frequency is commonly generated using acousto-optic modulators (AOM)<sup>7</sup> and Zeeman-lasers (ZL)<sup>8</sup>. However, other alternatives exist regarding single-sideband suppressed carrier (SSB-SC) modulation. In SSB-SC modulation, optical power is transferred from a carrier-frequency into another frequency, defined as the sideband. Alternatives include: rotating diffraction gratings<sup>9,10</sup> and mechanically rotating wave-plates.<sup>11-16</sup> Yet, the SSB-SC techniques described above are subject to certain drawbacks. AOM for instance, are not tunable because they are driven in resonance, and due to higher diffraction orders a large portion of the optical power is lost in the process (20%-30% when optimized). Zeeman lasers, on the other hand, are tunable, but optical power decreases rapidly as split-frequency increases, which limits the maximum target velocity and the amount of measurement axes in the application. Mechanically rotating diffraction-gratings and wave-plates are tunable and preserve optical power. However, due to mechanical vibrations, inertia, limited controllability and wear, these devices impose limitations on split-frequency and quality of the wavefront. In 1962,

Buhrer et al.<sup>17</sup> described a frequency modulator analog to mechanically rotating wave-plates, which utilizes the transverse Pockels effect to electro-optically modulate optical frequencies. This method of SSB-SC modulation promised modulation-frequencies orders of magnitudes higher than the mechanically rotating wave-plates. Moreover, using this technique, optical power is preserved, modulation-frequency can be electrically controlled and high sideband efficiencies can be achieved. Campbell<sup>18</sup> demonstrated sideband efficiencies of 95%+ at frequencies in the range of 10-100MHz. The initial goal of Campbell's research in electro-optic modulators was for utilization in telecommunication. However for various reasons, e.g. a too low bandwidth, the modulator proved not to be sufficiently practical. Sommargren<sup>19</sup> proposed this method to create split-frequencies for heterodyne interferometry, however until now the technique has not been researched in depth for this application.

In this publication a heterodyne displacement interferometer is demonstrated, which makes use of an electro-optically generated split-frequency. It is compared to state-of-the-art split-frequency generators in terms of periodic non-linearity (PNL)<sup>20</sup>. Additionally, the sideband efficiency of mechanical- and electro-optic rotating wave-plates is investigated. This publication starts with describing the physical principle of frequency shifting using rotating wave-plates. Consecutively, results of experiments using mechanically rotating wave-plates are displayed. Subsequently, the theory of the electro-optic effect in lithium niobate is treated, and verified by experiments. Eventually, the electro-optic frequency modulator is implemented in a heterodyne displacement interferometer, after which it is compared to state-of-the-art split-frequency generators and the obtained results are discussed.

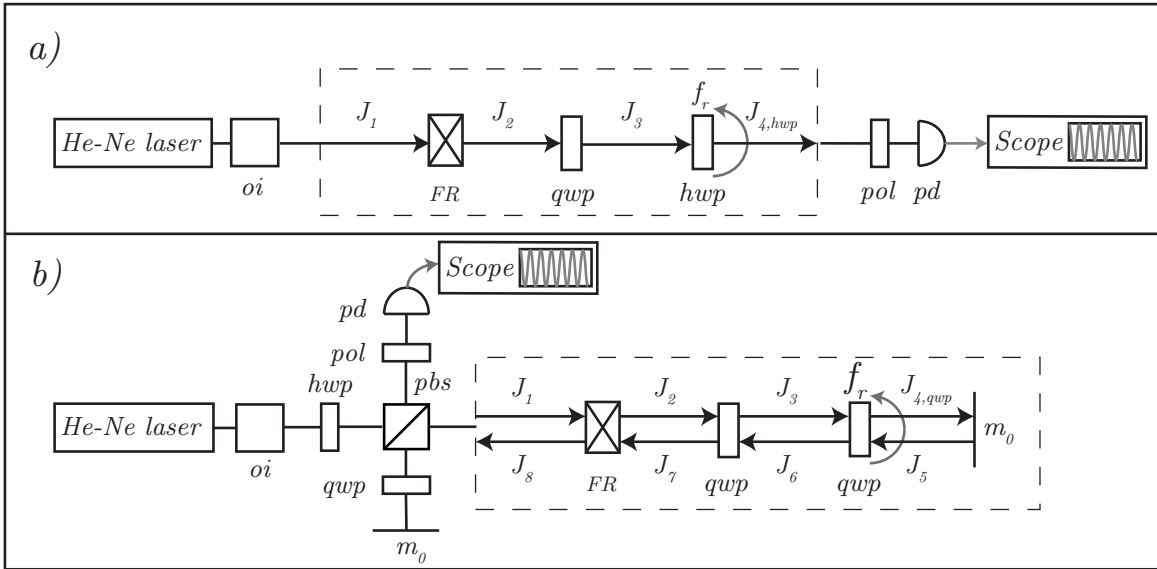


**Figure 1:** Optical set-ups used for experiments utilizing the mechanically rotating wave-plates. Subfigures a) and b) represent the set-ups used for the rotating half wave-plate and quarter wave-plate respectively. The states  $J_i$  in the dashed boxes relate to the Jones vector describing the polarization states, discussed in the main body of this manuscript. A Faraday rotator is added in the experiments for the rotating half wave-plate to create a theoretical similarity between both experimental setups. In the setup concerning the rotating half wave-plate, the Faraday rotator has no further useful functionality.

*Legend:* *oi*; optical isolator, *hwp*; half wave-plate, *pbs*; polarizing beam-splitter, *FR*; faraday rotator, *qwp*; quarter wave-plate, *m0*; mirror, *pol*; polarizer, *pd*; photo-detector

## II. Theory governing frequency shifting using rotating wave-plates

The act of frequency shifting using rotating waves-plates has been known for over a century<sup>21</sup> and is attributed to the angular Doppler effect.<sup>22</sup> Literature predominantly discusses rotating half-wave plates, however as explained in this section, SSB-SC modulation can be accomplished by both using half wave- and quarter wave-plates. To properly treat the theory, Jones calculus<sup>23</sup> is used to describe the polarization states, supported by a graphical representation shown in figure 1. This graphic displays the set-up and indicates the various intermediate stages in the frequency shifting process.

The Jones vector corresponding to state  $i$  in figure 1 is denoted as  $\mathbf{J}_i$ , while the optically modulating component's Jones matrix is denoted by  $\mathbf{M}_{cp}$ , where cp indicates the component's abbreviation.

When assuming a horizontal input polarization, the polarization state can be described using Jones Calculus, where  $\omega$  is defined as the optical frequency of the incident light.

$$\mathbf{J}_1 = \begin{bmatrix} 1 \\ 0 \end{bmatrix} e^{i\omega t} \quad (1)$$

The horizontal polarization is incident on a Faraday Rotator (FR) which rotates its polarization state by 45 deg. The Jones matrix of a FR is a rotational matrix denoted by  $\mathbf{R}(\theta)$ , where  $\theta$  is equal to the rotation angle.

$$\mathbf{M}_{FR} = \mathbf{R}(\theta) = \begin{bmatrix} \cos(\theta) & -\sin(\theta) \\ \sin(\theta) & \cos(\theta) \end{bmatrix} \quad (2)$$

$$\mathbf{M}_{FR} = \mathbf{R}\left(\frac{\pi}{4}\right) = \frac{1}{\sqrt{2}} \begin{bmatrix} 1 & -1 \\ 1 & 1 \end{bmatrix} \quad (3)$$

$$\mathbf{J}_2 = \mathbf{M}_{FR}\mathbf{J}_1 = \frac{1}{\sqrt{2}} \begin{bmatrix} 1 \\ 1 \end{bmatrix} e^{i\omega t} \quad (4)$$

Which is a linearly polarized light-wave with its polarization plane at 45 degrees from the horizontal, also called 'diagonal'. If a quarter-wave plate (QWP, i.e.  $\frac{\lambda}{4}$ ), with its fast axis parallel to the horizontal, is placed in series, a circularly polarized light-wave is obtained. The Jones matrix of a QWP with its fast axis parallel to the horizontal is described as:

$$\mathbf{M}_{\frac{\lambda}{4},90} = e^{i\frac{\pi}{4}} \begin{bmatrix} 1 & 0 \\ 0 & i \end{bmatrix} \quad (5)$$

Resulting in a left-handed circular (LCP) polarization state.

$$\mathbf{J}_3 = \mathbf{M}_{\frac{\lambda}{4},90}\mathbf{J}_2 = \frac{1}{\sqrt{2}} \begin{bmatrix} 1 \\ i \end{bmatrix} e^{i\omega t} \quad (6)$$

This LCP polarized light-wave is incident onto a rotating wave-plate, upon which it is modulated in frequency. The Jones matrix of the rotating wave-plate, rotating in opposite rotational direction of the LCP wave, is shown in equation 7.

$$\mathbf{M}_{wp} = \cos\left(\frac{\Gamma}{2}\right) \begin{bmatrix} 1 & 0 \\ 0 & 1 \end{bmatrix} + i \sin\left(\frac{\Gamma}{2}\right) \begin{bmatrix} \cos(2\omega_r t) & \sin(2\omega_r t) \\ \sin(2\omega_r t) & -\cos(2\omega_r t) \end{bmatrix} \quad (7)$$

Emergent from the wave-plate is an optical beam that, depending on the type of retardation plate, is either modulated into a single sideband or a combination of carrier- and sideband frequency.

$$\mathbf{J}_4 = \mathbf{M}_{\text{wp}} \mathbf{J}_3 =$$

$$\begin{aligned} & \cos\left(\frac{\Gamma}{2}\right) \begin{bmatrix} 1 \\ i \end{bmatrix} e^{i\omega t} + i \sin\left(\frac{\Gamma}{2}\right) \begin{bmatrix} \cos(2\omega_r t) + i \sin(2\omega_r t) \\ -i \cos(2\omega_r t) + \sin(2\omega_r t) \end{bmatrix} e^{i\omega t} \\ & = \cos\left(\frac{\Gamma}{2}\right) \begin{bmatrix} 1 \\ i \end{bmatrix} e^{i\omega t} + i \sin\left(\frac{\Gamma}{2}\right) \begin{bmatrix} 1 \\ -i \end{bmatrix} e^{i(\omega+2\omega_r)t} \end{aligned} \quad (8)$$

Note that for a rotating half-wave plate, the retardation  $\Gamma$  equals  $\pi$ , which implies the output light contains only a single sideband term with opposite circular polarization.

$$\mathbf{J}_{4,\text{hwp}} = \begin{bmatrix} 1 \\ -i \end{bmatrix} e^{i(\omega+2\omega_r)t} \quad (9)$$

When, instead of a half-wave plate, a wave-plate with a different retardation is rotated around its optical axis, the output spectrum contains a combination of carrier- and sideband frequencies. In this case, the rotating half wave-plate is substituted by a rotating quarter wave-plate.

$$\mathbf{J}_{4,\text{qwp}} = \cos\left(\frac{\Gamma}{2}\right) \begin{bmatrix} 1 \\ i \end{bmatrix} e^{i\omega t} + i \sin\left(\frac{\Gamma}{2}\right) \begin{bmatrix} 1 \\ -i \end{bmatrix} e^{i(\omega+2\omega_r)t} \quad (10)$$

When a mirror is placed at the output of the rotating quarter wave-plate, the circular polarizations reverses direction.

$$\mathbf{J}_5 = \cos\left(\frac{\Gamma}{2}\right) \begin{bmatrix} 1 \\ -i \end{bmatrix} e^{i\omega t} + i \sin\left(\frac{\Gamma}{2}\right) \begin{bmatrix} 1 \\ i \end{bmatrix} e^{i(\omega+2\omega_r)t} \quad (11)$$

Upon which the beam is once again incident on the rotating quarter-wave plate. From a photon's point of view, the apparent rotational velocity of the wave-plate is also reversed. Such that  $\omega_r t \rightarrow -\omega_r t$ . This changes the wave-plate matrix into the form shown in equation (12).

$$\mathbf{M}_{\text{wp}\dagger} = \cos\left(\frac{\Gamma}{2}\right) \begin{bmatrix} 1 & 0 \\ 0 & 1 \end{bmatrix} + i \sin\left(\frac{\Gamma}{2}\right) \begin{bmatrix} \cos(2\omega_r t) & -\sin(2\omega_r t) \\ -\sin(2\omega_r t) & -\cos(2\omega_r t) \end{bmatrix} \quad (12)$$

Emerging from the beam's second pass through the rotating quarter wave-plate are four terms. Containing terms in carrier-carrier, sideband-carrier, carrier-sideband and sideband-sideband.

$$\begin{aligned} \mathbf{J}_6 = \mathbf{M}_{\text{wp}\dagger} \mathbf{J}_5 &= \cos^2\left(\frac{\Gamma}{2}\right) \begin{bmatrix} 1 \\ -i \end{bmatrix} e^{i\omega t} - \sin^2\left(\frac{\Gamma}{2}\right) \begin{bmatrix} 1 \\ -i \end{bmatrix} e^{i\omega t} \\ &+ 2i \sin\left(\frac{\Gamma}{2}\right) \cos\left(\frac{\Gamma}{2}\right) \begin{bmatrix} 1 \\ i \end{bmatrix} e^{i(\omega+2\omega_r)t} \end{aligned} \quad (13)$$

The different terms interfere either constructively, or destructively to form the output spectrum.

$$\mathbf{J}_6 = \cos(\Gamma) \begin{bmatrix} 1 \\ -i \end{bmatrix} e^{i\omega t} + \sin(\Gamma) \begin{bmatrix} 1 \\ i \end{bmatrix} e^{i(\omega+2\omega_r)t} \quad (14)$$

As the quarter wave-plate exhibits a quarter wave-length retardation between its fast and slow-axis, i.e.  $\Gamma$  equals  $\frac{\pi}{2}$ . This results, ideally, into an optical beam that contains all the power in a single-sideband  $\omega + 2\omega_r$ .

$$\mathbf{J}_6 = \frac{1}{\sqrt{2}} \begin{bmatrix} 1 \\ i \end{bmatrix} e^{i(\omega+2\omega_r)t} \quad (15)$$

Note that the circular polarization direction is equal to the input polarization. Once again the light is incident on the quarter-wave plate, which restores it to its original 'diagonal' linear polarization. After which it is rotated another 45 degrees by the Faraday rotator.

$$\mathbf{J}_7 = \mathbf{M}_{\frac{\lambda}{4}} \mathbf{J}_6 = \frac{1}{\sqrt{2}} \begin{bmatrix} 1 \\ 1 \end{bmatrix} e^{i(\omega+2\omega_r)t} \quad (16)$$

$$\mathbf{J}_8 = \mathbf{M}_{\text{FR}} \mathbf{J}_7 = \begin{bmatrix} 0 \\ 1 \end{bmatrix} e^{i(\omega+2\omega_r)t} \quad (17)$$

This results into a polarization state that is orthogonal to the input polarization due to the non-reciprocal behavior of the Faraday rotator. Therefore, the input- and output beam can be separated using a polarizing beam-splitter.

A similar derivation can be performed if the rotational direction of the wave-plate rotates in the same direction as the electric-field vector of the circular polarization, resulting in a down shifted frequency sideband.

$$\mathbf{J}_{4\dagger,\text{hwp}} = \begin{bmatrix} 1 \\ -i \end{bmatrix} e^{i(\omega-2\omega_r)t} \quad \mathbf{J}_{8\dagger} = \begin{bmatrix} 0 \\ 1 \end{bmatrix} e^{i(\omega-2\omega_r)t} \quad (18)$$

When the stationary quarter wave-plate indicated in figure 1 is removed, and therefore a linear input polarization is incident on the rotating wave-plate, a  $4\omega_r$  signal is measured on the photo-detector. A linear polarization is a superposition of LCP and RCP polarization components of equal magnitude, resulting in an up-shifted term of  $2\omega_r$  and a down-shifted term of  $-2\omega_r$ , which interfere on the photo-detector, after passing a linear polarizer.

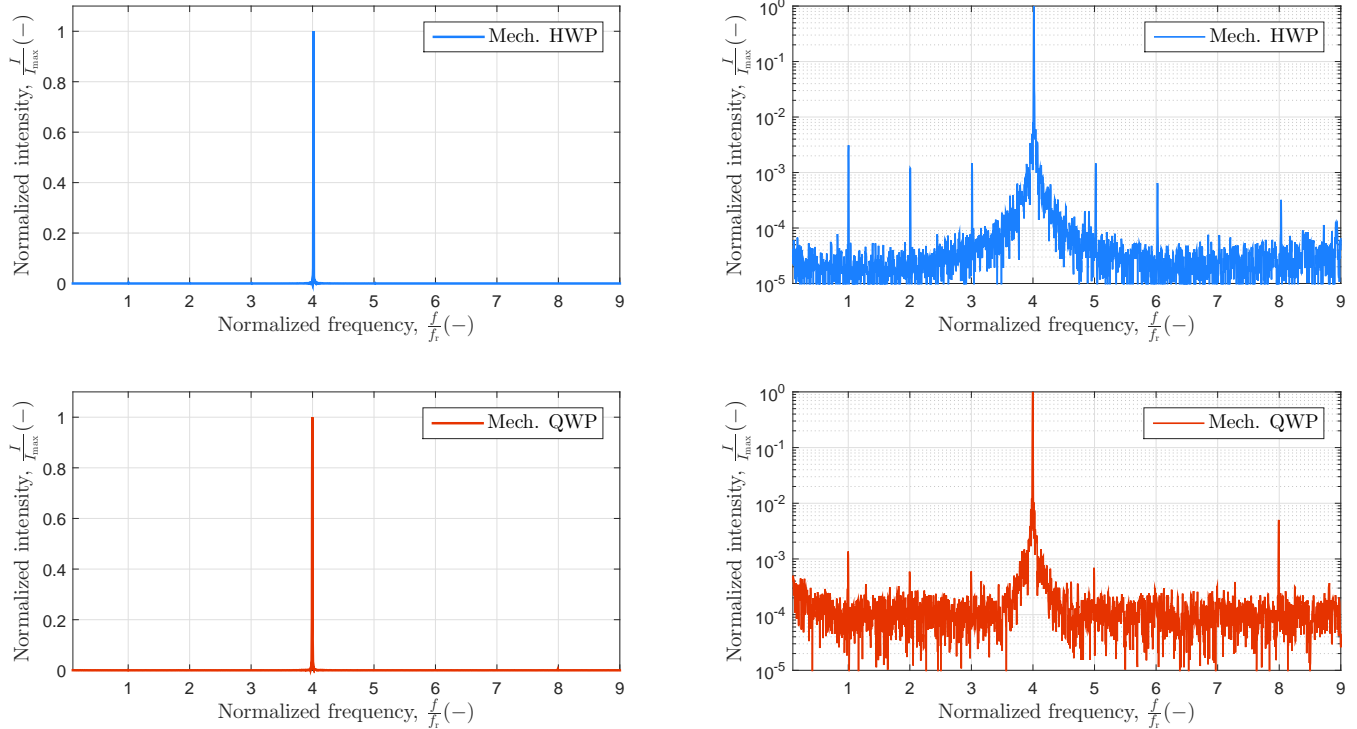


**Figure 2:** Experimentally measured beat spectrum for both the mechanically rotating half- and quarter wave-plate. A linear input polarization is incident on the wave-plates, rotating at  $f_r = 12.5\text{Hz}$ , to create the beat-spectrum. A flattop window has been applied in order to maximize the FFT amplitude accuracy.<sup>24</sup> The first column displays the spectrum on a linear scale, while the second column uses a log-scale to further investigate the various sidebands. The experimental data shows that sideband efficiencies  $\eta_{\text{sb}}$  of over 99% are present. However, due to the finite tolerances of the wave-plates and internal reflections, the beat spectrum displays optical power in other frequency bins as well. For instance, there are tolerances on the total respective retardation, angular alignment, and the orientation of the birefringent medium’s optic axis.

### III. Experimental results: Mechanically rotating wave-plates

In order to test the sideband efficiency of the described theory, a rotating wave-plate modulator has been built. This modulator consists of a DC-motor that drives a device containing the wave-plates, at a frequency  $f_r = 12.5\text{Hz}$ . Experiments have been performed using both a rotating half wave-plate, as well as a rotating quarter wave-plate. The experimental set-ups are displayed in figures 1a and 1b respectively. To properly investigate the output spectrum, a linear input polarization is used, as discussed in the previous section. Figure 2 displays the experimentally obtained beat spectra. In accordance with theory, in both experiments a  $4f_r$  beat frequency is measured. When the frequency content is plotted on a logarithmic scale, spurious frequency content in other sidebands can be investigated. The frequency content in these sidebands occurs due to internal reflections, tolerances in the wave-plate fabrication process and experimental setup. When the wave-plate does not exactly exhibit a retardation of  $\Gamma_{\text{hwp}} = \pi$  or  $\Gamma_{\text{qwp}} = \frac{\pi}{2}$ , frequency content appears in various other sidebands. Such retardation deviations occur due to a small error in the thickness of the wave-plate. Another possibility could be that the wave-plate is not specifically tuned for a 633nm

wavelength, but for a broader range, which due to the dependence of refractive index on frequency, imposes a different retardation. Moreover, when the optic axis of the wave-plate is not perfectly orthogonal to the input beam, spurious frequency content in other sidebands is present. This can occur due to misalignment of the wave-plate, or an imperfect rotation around its optical axis.

A sideband efficiency can be introduced, which is a measure for the SSB-SC performance of the wave-plates. This sideband efficiency determines the amount of optical power in the expected sidebands, relative to the total optical power in the signal. In this case, the FFT’s amplitude resolution is an important factor to determine the sideband-efficiency, therefore a flattop window has been applied to the data.<sup>24</sup> The definition of sideband efficiency is expressed in equation 19, where  $\omega_i$  corresponds to frequency bins resembling integer multiples of the normalized frequency.

$$\eta_{\text{sb}} = \frac{A(\omega_4)}{\sum_{k=0}^{\infty} A(\omega_k)} \quad (19)$$

Frequency bins that resemble an amplitude inside the  $3\sigma$  (99.7%) noise range have not been included in the calculation. Applying this expression to the data, the sideband efficiencies result in  $\eta_{\text{sb,hwp}} = 99.1\%$  and  $\eta_{\text{sb,qwp}} = 99.2\%$

#### IV. Theory governing the electro-optic wave-plate

Research in the early 1960s showed that wave-plates can also be induced electro-optically. By applying an electric field to a certain electro-optic medium, the refractive indices of the material change accordingly, creating a wave-plate. Whenever this electric field is rotated, this medium acts as a rotating wave-plate. Using electric fields, relatively high rotational frequencies can be achieved, which makes it suitable for heterodyne displacement interferometry. Such electro-optic rotating wave-plates can be induced in materials that lack inversion symmetry, and belong to the 3m-crystal group, exhibiting a c-axis. Lithium niobate<sup>25</sup> is such a material. Moreover it displays a large electro-optic coefficient, is transparent to light in the range of 420-5200 nm wavelength, and is a widely applied material in the field of optics.

The change in refractive index under the influence of an electric field can be described by using components  $r_{ij}$  of the electro-optic tensor  $\mathbf{r}$  and components  $E_j$  of the electric-field vector  $\mathbf{E}$ .

$$\frac{1}{n_i^2} = \left( \frac{1}{n_i^2} \right)_{\mathbf{E}=0} + \sum_{j=1}^3 r_{ij} E_j \quad (20)$$

The refractive indices of a birefringent crystal are most often expressed using an index ellipsoid. A right-handed orthogonal coordinate system is defined, shown in figure 3a). As light travels along the optic axis of the crystal, which corresponds to the direction of the z-axis, the refractive indices and allowed polarization directions are defined by the xy-plane index ellipse, which is described mathematically by equation 21.

$$\left\{ \frac{1}{n_o^2} + (r_{11}E_x - r_{22}E_y) \right\} x^2 + \left\{ \frac{1}{n_o^2} + (r_{22}E_y - r_{11}E_x) \right\} y^2 - 2(r_{22}E_x + r_{11}E_y)xy = 1 \quad (21)$$

This equation can be written in terms of index ellipse' principal axes by performing a rotational transformation around an angle  $\theta$ , as shown in equation 22.

$$\theta(t) = \frac{1}{2} \arcsin \left\{ \frac{-r_{22}}{\bar{r}} \cos(\alpha) - \frac{r_{11}}{\bar{r}} \sin(\alpha) \right\} = -\frac{1}{2}(\alpha + \Psi) \quad (22)$$

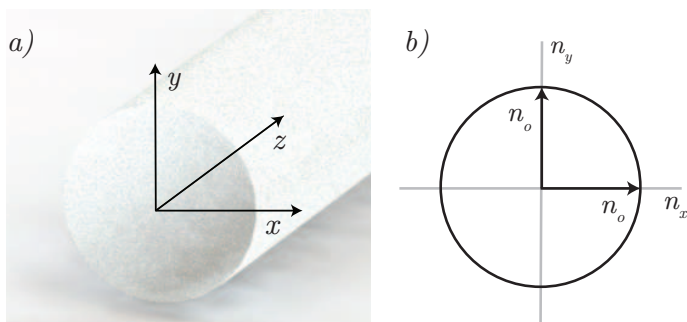


**Figure 3:** a) Lithium niobate crystal rod, indicating the chosen coordinate axes. The optic axis of the material corresponds to the z-direction. b) Index ellipse in the absence of an electric field. No birefringence is present, as light travels along the optic axis of the crystal.

Where  $\alpha$  describes the phase of the electric field at a drive frequency  $f_{EF}$ , measured in cycles per second.

$$\alpha = 2\pi f_{EF}t \quad \bar{r} = \sqrt{r_{11}^2 + r_{22}^2} \quad \Psi = \arcsin\left(\frac{r_{22}}{\bar{r}}\right) \quad (23)$$

From these equations it can be derived that, in case of a rotating electric field, the principal axes of the index ellipse rotate in the opposite direction of the electric field, at half the frequency (!). This process is represented graphically in figure 4. The respective retardation  $\Gamma$  between waves traveling along the slow and fast axis of the index ellipse is described by equation 24.

$$\Gamma = \frac{2\pi L n_o^3 \bar{r} E_m}{\lambda} \quad (24)$$

Where  $L$  is the length of the crystal (m),  $n_o$  is the ordinary refractive index,  $E_m$  is the electric field magnitude ( $\text{Vm}^{-1}$ ) and  $\lambda$  is the free-space wavelength (m). In order to induce a half-wave plate or quarter-wave plate, the retardation  $\Gamma$  equals  $\Gamma_{\text{hwp}} = \pi$  or  $\Gamma_{\text{qwp}} = \frac{\pi}{2}$  respectively, which defines half- and quarter-wave voltage, indicated in equations 25 and 26.

$$V_\pi = \frac{\lambda d}{2Ln_o^3 \bar{r}} \quad (25) \quad V_{\frac{\pi}{2}} = \frac{\lambda d}{4Ln_o^3 \bar{r}} \quad (26)$$

A similar derivation as demonstrated for the mechanical wave-plates can be performed, to conclude frequency shifting with electro-optic wave-plates is possible as well. Utilizing this electro-optic technique, rotational frequencies can be obtained that are orders of magnitude higher than mechanically rotating wave-plates. It can be easily shown that if an incident circularly polarized light beam enters the crystal, it is up-shifted by a frequency  $f_{EF}$  if its polarization direction is rotating in the same direction as the electric field and therefore in opposite direction of the index ellipse. In contrast, a circularly polarized beam that exhibits its polarization direction opposite to that of the rotating electric field is down-shifted by  $f_{EF}$ .

#### Electro-optic vs. Elasto-optic

*It should be noted that although the electro-optic rotating wave-plate is based on the electro-optic effect, where the change in refractive index is directly influenced by the electric field vector, every material that exhibits the electro-optic effect is per definition a piezo-electric material. Through electrostriction and the converse piezoelectric effect, strains in the material are introduced. These strains cause a change in refractive index by means of the elasto-optic effect, which is an indirect-effect of the electric field vector. As the optical frequency shifting technique is based on the electro-optic effect only, such strains are undesired and should therefore be avoided. The extra term as a result of the elasto-optic effect is shown in equation 27*

$$\frac{1}{n_i^2} = \underbrace{\left( \frac{1}{n_i^2} \right)_{\mathbf{E}=0}}_{\text{Inherent index ellipse}} + \underbrace{\sum_{j=1}^3 r_{ij} E_j}_{\text{Electro-optic effect}} + \underbrace{\sum_{j=1}^3 \sum_{k=1}^3 p_{ijk} u_{jk}}_{\text{Elasto-optic effect}} \quad (27)$$

$$\left\{ \frac{1}{n_o^2} + (r_{11}E_x - r_{22}E_y) \right\} x^2 + \left\{ \frac{1}{n_o^2} + (-r_{11}E_x + r_{22}E_y) \right\} y^2 - 2(r_{22}E_x + r_{11}E_y)xy = 1$$

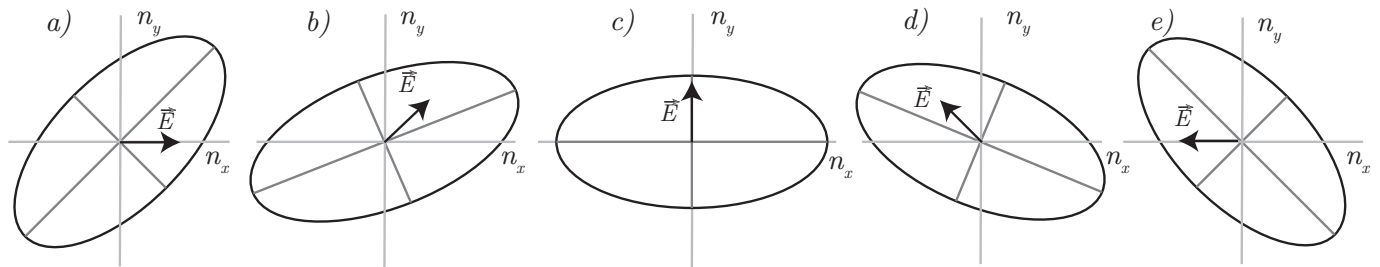


**Figure 4:** Graphical representation relating the electric field vector to the principal axes of the index ellipse, mathematically described in equation 21. Note that the principal axes rotate in the opposite direction of the electric field, at half the frequency. An initial offset  $\frac{1}{2}\Psi = -\frac{\pi}{4}$  is present, as shown in the first graphic.

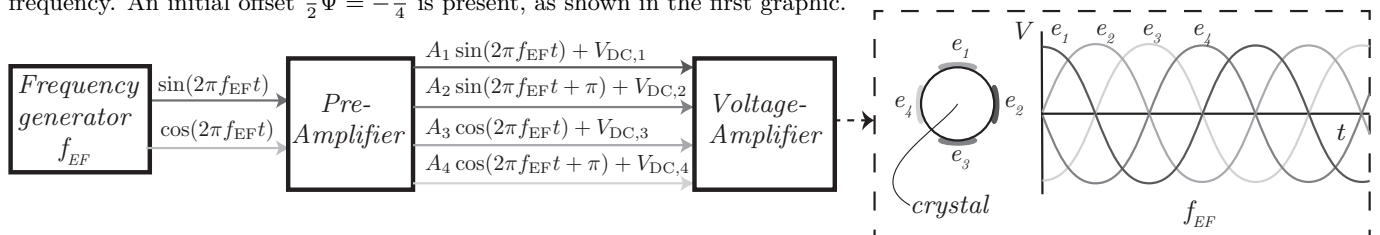


**Figure 5:** Schematic overview of the setup regarding the electronics. A sine and a cosine waveform are generated by the frequency generator at a frequency  $f_{EF}$ . These signals are fed into a pre-amplifier, which outputs four waveforms, phase shifted 90 degrees respectively. In addition, the gain  $A_i$  and DC offset  $V_{DC,i}$  of each channel can be controlled to account for setup maladjustments and possible residual strains inside the crystal, resulting from the fabrication process.

## V. Design considerations

In this section, the main design considerations of an electro-optic modulator are discussed. This includes the generation of a homogeneous rotating electric field, acoustic resonances, acousto-optic diffraction and set-up maladjustments.

### Rotating Homogeneous Electric Field

To properly induce an electro-optic rotating wave-plate, a homogeneous rotating electric-field has to be present across the entire cross-section of the beam's pass through the crystal. Such a homogeneous field can be generated by various electrode configurations subject to phase-shifted alternating voltages. The most straightforward solution is to place 4 electrodes, mutually separated around the crystal by 90 degrees, upon which a sine and cosine voltage signal are imposed, as shown in figure 5. An overview of various electrode configurations, along with their electric field homogeneity, is shown in figure 6. From these simulations it can be concluded that although wider electrodes account for a larger homogeneous electric field, the electric field gradients on the corners of the crystal are considerably larger.

### Acoustic Resonances & Acousto-Optic Diffraction

Electric-field gradients inside the crystal introduce undesired mechanical strains, acoustic waves and resonances, by means of the converse piezoelectric effect. These parasitic effects are undesired and can strongly influence the performance of the modulator<sup>26</sup>. The influence of the crystal strains and resonances could dominate the total change in refractive index at the moment the crystal is driven in one of its resonance frequencies. To prevent this from happening, the electric-field driving frequency should be chosen far from any resonance frequencies<sup>26</sup>. An eigenfrequency analysis is performed to indicate the resonances of the crystal, shown in figure 7. According to this analysis a suitable driving frequency can be determined. Whenever the driving field frequency is near any of such resonances, a large amount of energy is absorbed by the lithium niobate crystal.<sup>27</sup> The total energy that is coupled into the  $k^{\text{th}}$  harmonic of a certain vibration mode, varies as  $(\frac{1}{k^2})$ .<sup>28</sup> Therefore, resonances of the higher harmonics are less influential on the performance of the modulator. In addition to acoustic resonances, the acousto-optic effect can be responsible for a loss in optical power at the output of the crystal. Elastic waves inside the crystal, introduce a 'grating-like' behavior similar to the working principle of AOMs, which diverts a portion of the optical power away from the main beam at well defined diffraction orders.<sup>29</sup>

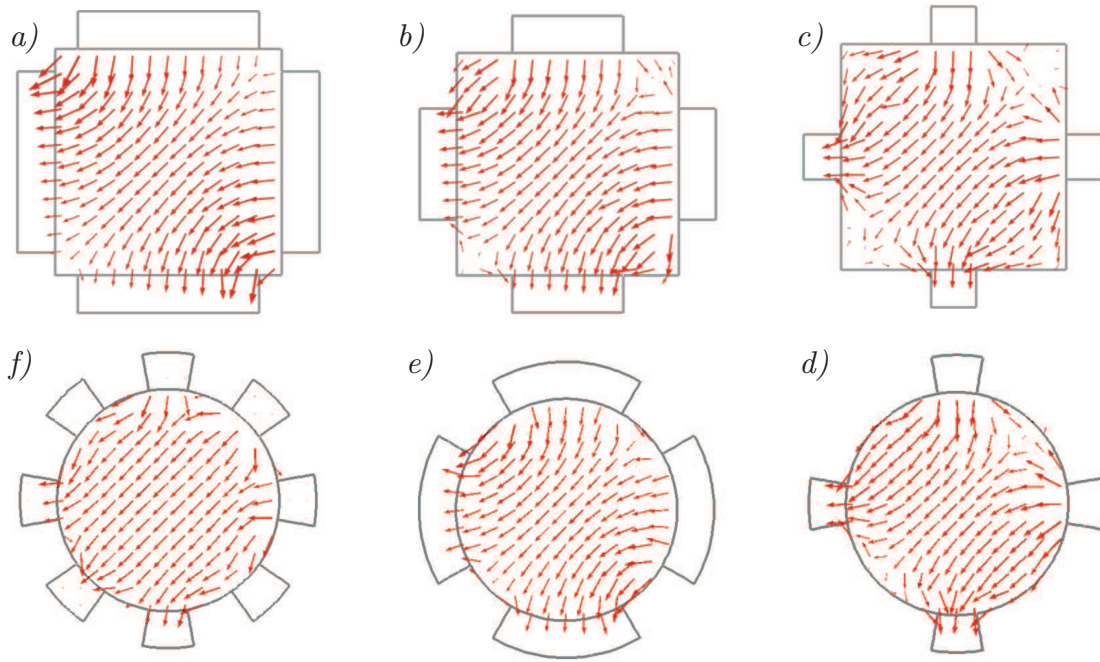


**Figure 6:** Graphical representation of the electric-field distribution for various electrode configurations and crystal geometries. The dimension regarding electrode thickness is scaled up for proper visualization. Simulations are performed at a time instant  $t = \frac{T_{EF}}{8}$ , at this time all the electrodes are charged with the same voltage amplitude. The phase of the electric-field vector indicates the direction of the electric-field, while the length indicates the logarithmic amplitude of the field. It can be seen that for wider electrodes, the field homogeneity is larger, however higher gradients are present in the corners of the lithium niobate crystal. Subfigure f) displays a simulation containing 8 electrodes, of which the applied voltages are mutually out of phase by 45 deg, this drastically increases the homogeneity of the electric field. The electrode configuration displayed in subfigure e) was used for the experiments in this publication.

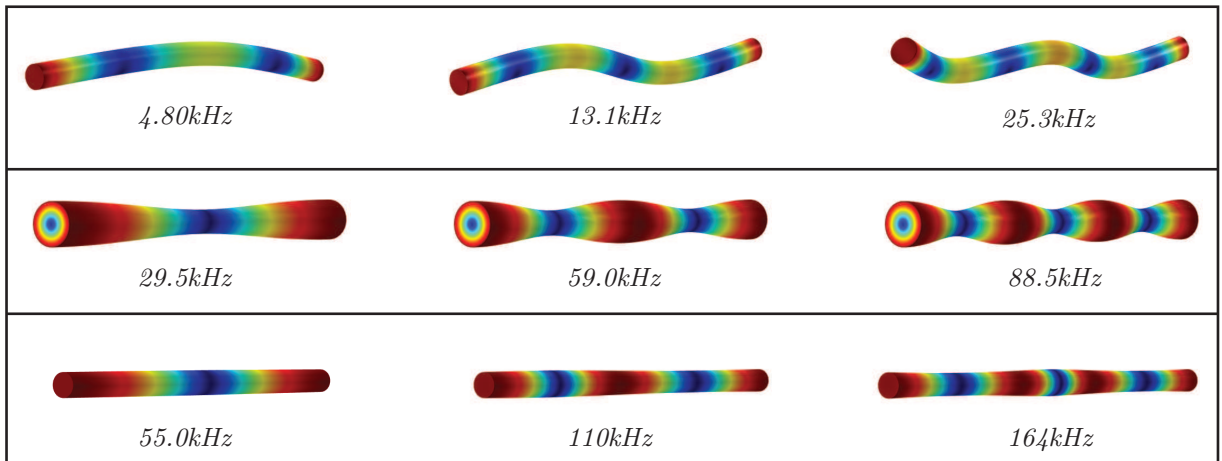


**Figure 7:** Vibrational modes of a free lithium niobate  $3\varnothing \times 60\text{mm}$  crystal rod. The figure shows the three fundamental modes and their higher harmonics. Indicated by color is the total displacement, where red illustrates a large displacement and blue indicates a small displacement. Note that these modes can be scaled arbitrarily. The eigenfrequency accompanied by the particular mode is indicated underneath the specific figure.

### Thermal dissipation

While the electric-field vector is rotating inside the lithium niobate crystal, it induces oscillating motions of the charged particles. Such charged particle oscillating motions are responsible for a current inside the crystal, alternating with a frequency equal to the driving frequency  $f_{\text{EF}}$ . The total power absorbed by the crystal, originating from charged particle oscillations can be well approximated by the expression shown in equation 28.<sup>30</sup>

$$P = 2\pi \iiint_V f_{\text{EF}} \varepsilon \tan(\Phi) \mathbf{E} \cdot \mathbf{E} dV \quad (28)$$

Where  $f_{\text{EF}}$  defines the electric-field frequency,  $\varepsilon$  the permittivity of lithium niobate,  $\tan(\Phi)$  the loss tangent and  $\mathbf{E} \cdot \mathbf{E}$  the electric field amplitude squared. Representative values for the loss tangent in lithium niobate equal  $\tan(\Phi) = 0.01 - 0.1$ , however this quantity varies widely as a function of frequency and temperature.<sup>31</sup> The increase in temperature inside the crystal accounts for a defocussing and upward deflection of the beam, as the ordinary refractive index of lithium niobate is a function of temperature.<sup>32</sup> The electro-optic coefficient  $\bar{r}$  can be assumed to be independent of temperature at temperatures below  $100^\circ\text{C}$ .<sup>33</sup>, therefore the half- or quarter-wave electric field magnitude is constant. From equation 28 it can be easily derived that, for an equal aspect ratio ( $dL^{-1}$ ), a smaller crystal is beneficial in terms of power dissipation. Moreover, by utilizing the double-pass operation with the according quarter-wave voltage, the power dissipation is one quarter of that of the single pass using the half-wave voltage.

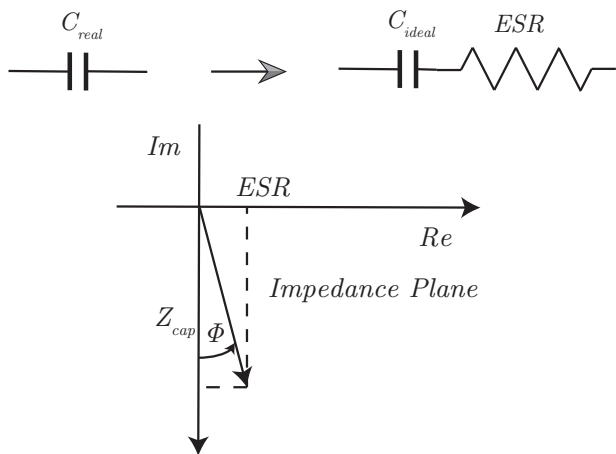


**Figure 8:** Loss tangent of a non-ideal capacitor indicated in the impedance plane. Every practical capacitor has a non-zero equivalent series resistance (ESR), thereby dissipating heat inside the capacitor. The ratio of the ESR over the imaginary impedance  $Z_{\text{cap}}$  is defined as the loss tangent,  $\tan(\Phi)$ . The total power dissipated inside a capacitor is well approximated by equation 28.

### Setup maladjustments

Similar to the mechanically rotating wave-plates, the electro-optic modulator suffers from a non-ideal SSB-SC modulation, due to various error sources. Campbell (1971)<sup>18</sup>, provided an overview by means of a theoretical approach, to determine which error sources cause certain spurious frequency modulation. Table I displays an overview of the various error sources, and solutions to solve these potential error sources.

**Table I:** Setup maladjustments accompanied by the measures taken to minimize their influence

Maladjustment	Solution
Field-magnitude error	Tunable voltage amplitude
Amplitude imbalance	Tunable amplification (p.c.)
Phase imbalance	Tunable phase relation
DC-bias in drive-field	Tunable DC-offset (p.c.)
Electrodes misaligned to c-axis (-)	
Reversed CP input-beam	High-quality QWP
Optical beam relative to c-axis	4-DOF positioning stage

(p.c.) indicates 'per channel'. A single channel represents an individual electrode, in total four mutually independent channels are present in the electrical setup, as shown in figure 5.

### Origin of PNL and the relation to non-ideal SSB-SC

Traditionally, periodic non-linearity (PNL) in heterodyne displacement interferometers originates from frequency-leakage during the frequency-separation of the coaxial optical beam.<sup>34,35</sup> This PNL-error can be reduced significantly using spatially separated heterodyne beams, hence enhancing measurement linearity.<sup>36</sup>

The maladjustments listed in table I, directly influence the sideband efficiency in the SSB-SC modulation. Such imperfect modulation introduces multiple frequencies in the optical beam traveling to the target. These multiple frequencies superimpose, to create a non-linear periodic error on the obtained displacement data, limiting the measurement accuracy. For a heterodyne interferometer with spatially separated optical paths, PNL due to frequency-separation is minimal. Hence, the most dominant error sources are expected from a non-ideal SSB-SC modulation and ghost-reflections in the system. PNL-errors due to ghost-reflections and frequency-leakage are present at specific frequencies, represented by equation 29. Where  $k$  indicates the PNL-order,  $N$  the interferometer's fold factor (i.e. the number of times the beam traverses forth and back the target mirror),  $v_{\text{target}}$  the target's velocity ( $\text{ms}^{-1}$ ) and  $\lambda$  the free-space wavelength (m) of the optical beam.

$$f_{\text{PNL}} = \frac{kNv_{\text{target}}}{\lambda} \quad (29)$$

## VI. Modulator design and experimental setup

The rotating electro-optic wave plate consists of four 1x60mm (width  $\times$  length) copper electrodes mutually spaced 90 deg on the circumference of a  $\varnothing$ 3x60mm c-cut lithium niobate crystal rod, as shown in figure 5. Both crystal facets are polished and anti-reflection (AR) coated to minimize external and internal reflections. The modulator is placed on a 4 DOF positioning stage to properly align the crystal to the incident light-beam, enhancing modulator performance. A photograph of the electro-optic modulator is shown in figure 9. Alternating voltages are imposed over the two orthogonal axes of the cross-section, composed of a sine and cosine signal respectively.

$$V_x = V_0 \cos(\omega_r t) \quad V_y = V_0 \sin(\omega_r t)$$

For a He-Ne laser  $\lambda = 633\text{nm}$ , a  $\varnothing$ 3x60mm lithium niobate crystal exhibiting an ordinary refractive index of  $n_o = 2.286$  and an electro-optic coefficient  $\bar{r} = 3.4 \cdot 10^{-12} \text{ mV}^{-1}$ , the theoretical half- and quarter-wave voltages equal:

$$V_\pi = 389.5\text{V} \quad V_{\frac{\pi}{2}} = 194.8\text{V}$$

The crystal is driven by an electric-field frequency  $f_{\text{EF}} = 20\text{kHz}$ . Hence, the thermal power absorbed by the crystal is calculated as  $P_{\text{th}} = 15\text{mW}$ , which is negligibly small. An overview of the various components and measurement instruments present in the experimental setup is shown in table II.

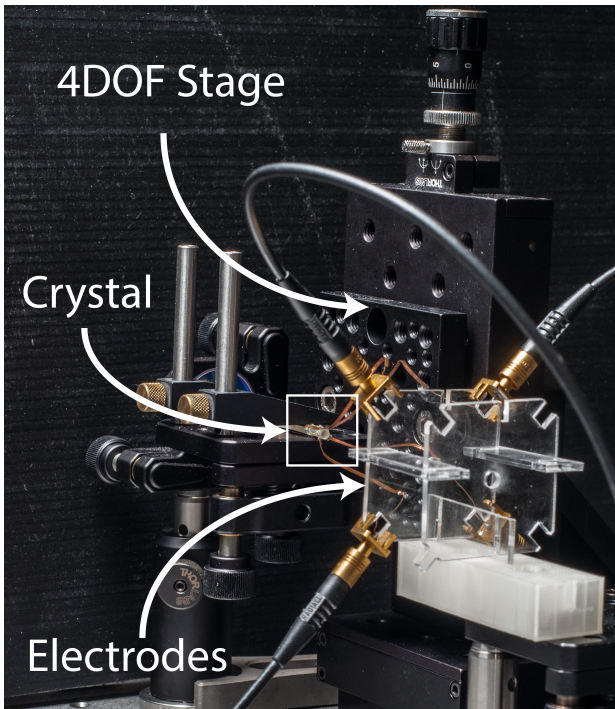


**Figure 9:** Photograph of the electro-optic rotating wave-plate modulator. The  $\varnothing$ 3x60mm c-cut lithium niobate rod is placed on a 4 DOF positioning stage and is surrounded by four electrodes, mutually spaced by 90 degrees.

**Table II:** Overview of the most important components regarding the electro-optic experimental setup.

Component	Properties
Crystal	C-cut LiNbO <sub>3</sub> $\varnothing$ 3 $\times$ 60 mm
Laser type	633nm Thorlabs HR S015
Electrodes	Copper 1x0.1x60 mm ( $w \times t \times L$ )
Function generator <sup>(I)</sup>	HP Model 203A/Agilent 33220A
Pre-amplifier <sup>(II)</sup>	In-house developed
Voltage-amplifier <sup>(III)</sup>	In-house developed
Photo-detector	PDA36A-EC
Data-acquisition	NI-USB6211
Lock-in amplifier	SRS Model SR830
1DOF Precision-stage	Aerotech ABL1000
LPF Bessel/Butterworth	Krohn-Hite Model 3362
Frequency-mixers	MiniCircuits ZAD-1-1+
1DOF IF Optical monolith	Agilent E1826G

<sup>(I)</sup> *HP*: Variable phase function generator. 2-channel output, relative phase arbitrarily tunable. 60kHz bandwidth.

*Agilent*: Digital 20MHz bandwidth function generator

<sup>(II)</sup> 2 port input, 4 port output. The gain and DC-offset of each channel can be individually tuned. See figure 5

<sup>(III)</sup> 40x amplification factor, maximum output voltage; 200V per channel. The bandwidth equals 200kHz

## VII. Experimental results: Electro-optic stationary wave-plate

In order to verify the working principle of the electro-optic wave-plate, a stationary electro-optic wave-plate has been created as a first experiment. This stationary wave-plate was induced by applying a DC electric potential across the lithium niobate crystal and is analogous to an electro-optic modulator (EOM). In the following subsections, both a stationary electro-optic half- and quarter wave-plate are induced, by utilizing a single- and double-pass operation respectively.

### Electro-optic stationary half wave-plate

The experimental set-up regarding the stationary electro-optic half wave-plate, is shown in figure 10. When the voltage applied to the crystal equals zero, no birefringence is present, therefore the crossed polarizers block light from reaching the photo-detector (PD). This experiment can also be used as an alignment-tool. Only if the crystal is aligned properly, no optical power is incident on the photo-detector. As the DC-voltage is increased, the light traveling through the crystal suffers from birefringence, which alters the polarization state. This results in a certain amount of the optical power passing the second polarizer, after which it is incident on the photo-detector. The intensity incident on the PD reaches a maximum at the half-wave voltage  $V_\pi$ . Experimental results of the described set-up are displayed in figure 11. From the experiments, the stationary half-wave voltage  $V_\pi$  is derived to be  $V_\pi = 342.5 \text{ V}$

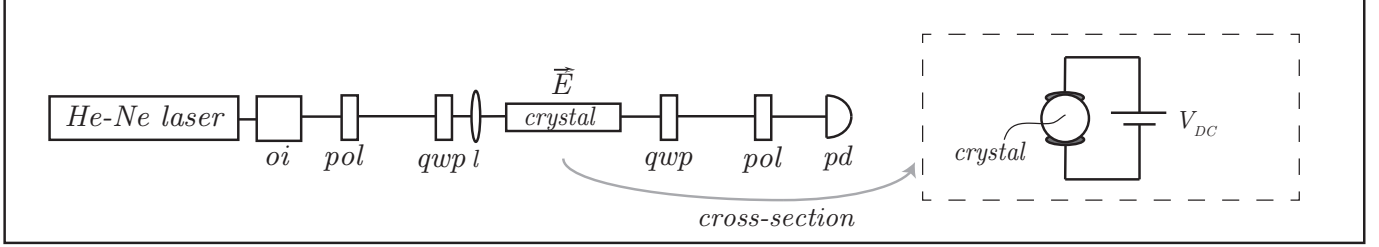


**Figure 10:** Experimental set-up used for creating a stationary electro-optic wave-plate in single-pass operation.  
 Legend: oi; optical isolator, l; lens, qwp; quarter wave-plate, crystal; c-cut lithium niobate rod, pol; polarizer, pd; photo-detector

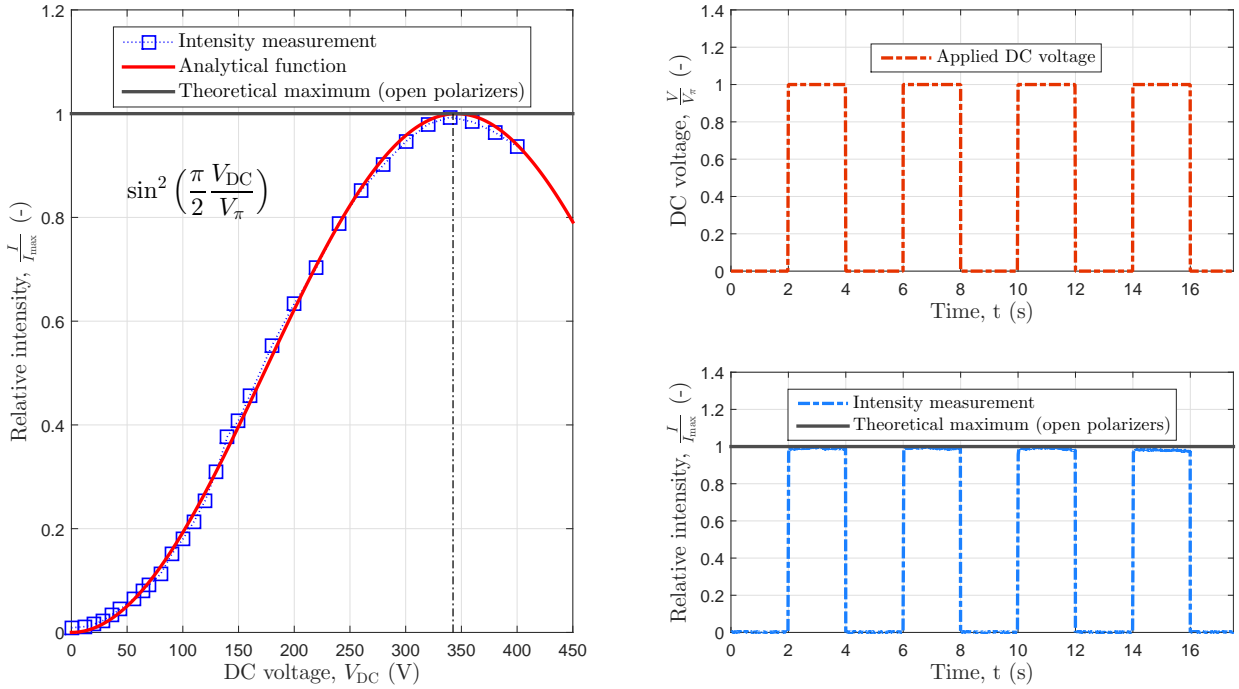


**Figure 11:** Experimental results regarding the stationary electro-optic waveplate in single-pass operation. The left figure indicates the light-intensity incident on the photo-detector, relative to the theoretical maximum, as a function of the applied DC-voltage. The theoretical maximum is defined as the amount of optical power incident on the PD when the polarizers are both 'open', instead of crossed. A maximum is expected at the half-wave voltage  $V_\pi$ , experimentally determined at 341V. When this half-wave voltage is surpassed, the incident intensity decreases as expected. The maximum DC-voltage applied is limited by the voltage amplifier at 400V. The right figures indicate a switched mode operation, switching the intensity to a maximum and minimum at a period  $T = 4\text{s}$ . Where the applied DC-voltage represents a square wave at the half-wave voltage  $V_\pi$  exhibiting a duty cycle of 50%.

### Electro-optic stationary quarter wave-plate

As shown in section II, by utilizing a double pass operation, a quarter wave-plate can also serve as an optical frequency shifter. This would require only half the electric potential, which has an advantage in terms of required voltage amplification and power absorption of the crystal. The set-up used for demonstrating an electro-optically induced stationary quarter wave-plate is shown in figure 12. Due to the double-pass operation, the total respective retardation between the fast and slow wave is doubled. Therefore, the DC-voltage required to reach a maximum intensity on the photo-detector is half that of the single-pass operation. The experimental results are shown in figure 13, displaying a double frequency with respect to the electro-optically induced half wave-plate. From the experiments, the quarter-wave voltage is determined at  $V_{\frac{\pi}{2}} = 164$  V. This value is slightly lower than expected w.r.t. the half-wave voltage in single-pass operation, which is most likely due to the alignment of the optical beam w.r.t. the electric-field in the crystal.

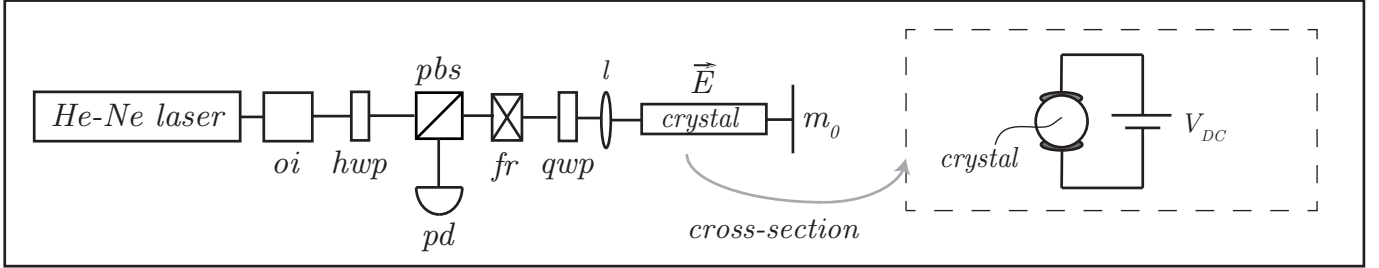


**Figure 12:** Experimental set-up used for creating a stationary electro-optic wave-plate in double-pass operation. Legend: *oi*; optical isolator, *hwp*; half wave-plate, *pbs*; polarizing beam-splitter, *fr*; Faraday rotator, *qwp*; quarter wave-plate, *l*; lens, *crystal*; c-cut lithium niobate rod, *m<sub>0</sub>*; mirror, *pd*; photo-detector

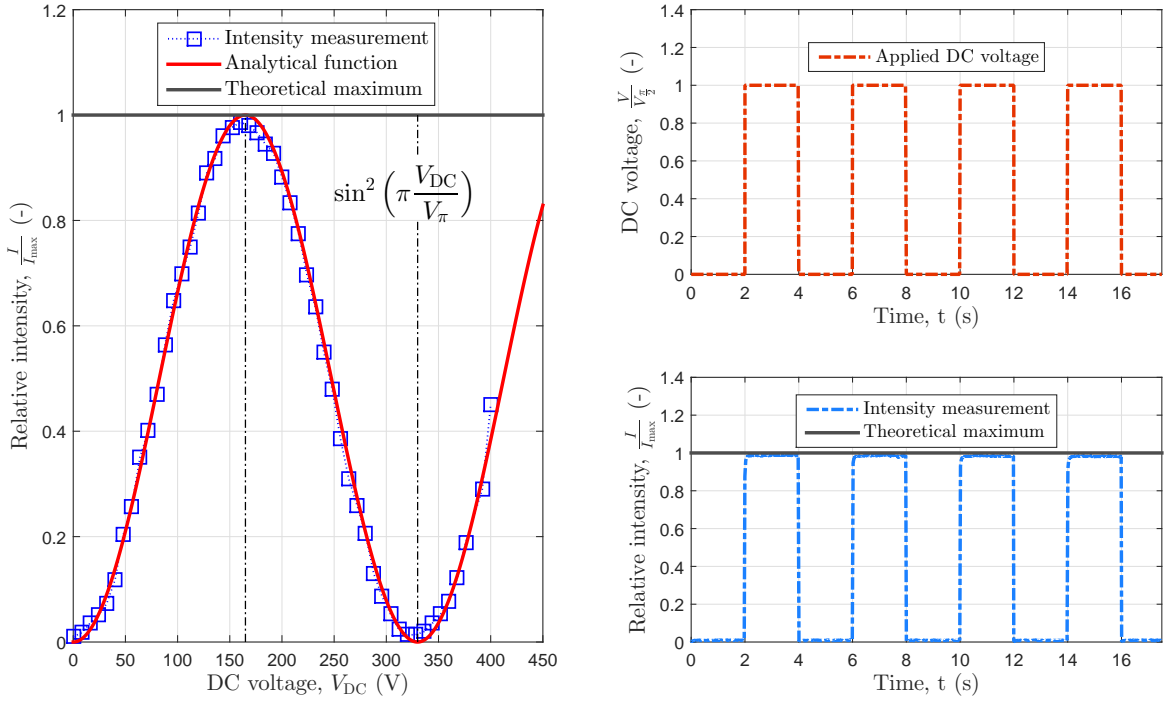


**Figure 13:** Experimental results regarding the stationary electro-optic quarter wave-plate. The left figure indicates the light-intensity incident on the photo-detector, relative to the theoretical maximum, as a function of the applied DC-voltage. The theoretical maximum is defined as the amount of optical power incident on the PD, when the crystal is substituted by a stationary quarter wave-plate. A maximum is expected at the quarter-wave voltage  $V_{\frac{\pi}{2}}$ , experimentally determined at 164V. When this quarter-wave voltage is surpassed, the incident intensity decreases as expected, until the half-wave voltage is reached at which the stationary wave-plate serves as a full wave-plate. Therefore no light is incident on the photo-detector. The maximum DC-voltage applied is limited by the amplifier at 400V. The right figures indicate a switched mode operation, switching the intensity to a maximum and minimum at a period of  $T = 4$  s. Where the applied DC-voltage represents a square wave at the quarter-wave voltage  $V_{\frac{\pi}{2}}$ , exhibiting a duty cycle of 50%.

### VIII. Experimental results: Electro-optic rotating quarter wave-plate

In this section, the sideband efficiency of the experimental modulator is investigated. An optical setup is established, which is similar to the reference beat signal in a heterodyne displacement interferometer. This setup is shown in figure 14. In this setup, half of the optical power is reflected by the polarizing beam-splitter, while the other half travels through the electro-optic rotating quarter-wave plate. After reflection, both optical beams interfere on the photo-detector, such that the sideband efficiency can be determined. The crystal is driven at a frequency  $f_{\text{EF}} = 20\text{kHz}$ , creating a 20kHz beat-signal on the photo-detector. Furthermore, the quarter-wave voltage is experimentally determined at 385V, deviating from theory by a large percentage. In these experiments, acousto-optic diffraction was not observed, neither was a strong frequency-dependence resulting from mechanical resonances of the crystal. The experimental results are shown in figure 17, displaying a sideband efficiency of  $\eta_{\text{eo,qwp}} = 97.1\%$ . Optical power in higher sidebands is observed, attributed to the error sources listed in table I. Tunability of the various electronic components proved very convenient to minimize this spurious frequency content. DC-offsets in the electronic signals turned out to be of minimal necessity, as the residual strains inside the crystal were negligibly small. The ability to continuously tune the phase between the electrical waveforms was of great relevance, because the sensitivity of sideband efficiency w.r.t. phase is relatively large.

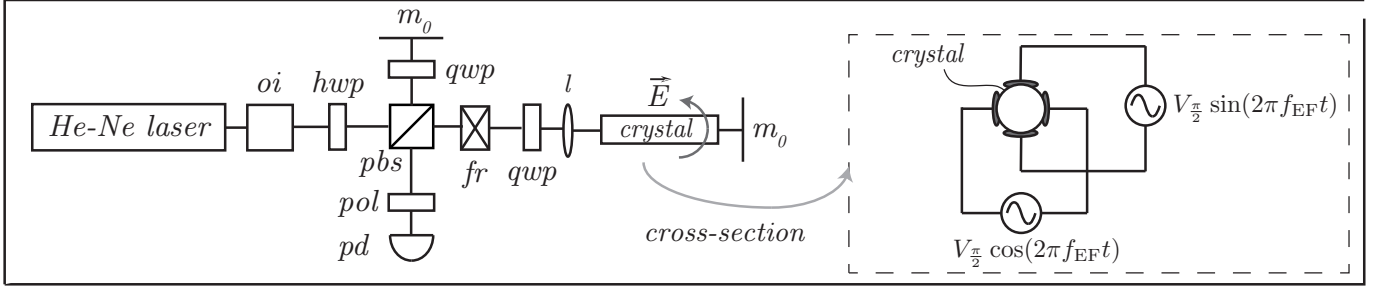


**Figure 14:** Optical set-up used for experiments regarding the electro-optic rotating quarter wave-plate. In this experiment half of the light intensity is reflected by the polarizing beam-splitter, while the other half travels through the modulator. After reflection, the light-beams interfere on the photo-detector creating a beat-signal at the electric-field rotating frequency. The crystal is driven at an electric field frequency  $f_{\text{EF}} = 20\text{kHz}$ .

Legend: *oi*; optical isolator, *hwp*; half wave-plate, *pbs*; polarizing beam-splitter, *fr*; Faraday rotator, *qwp*; quarter wave-plate, *l*; lens, *crystal*; *c-cut lithium niobate rod*,  $m_0$ ; mirror, *pol*; polarizer, *pd*; photo-detector

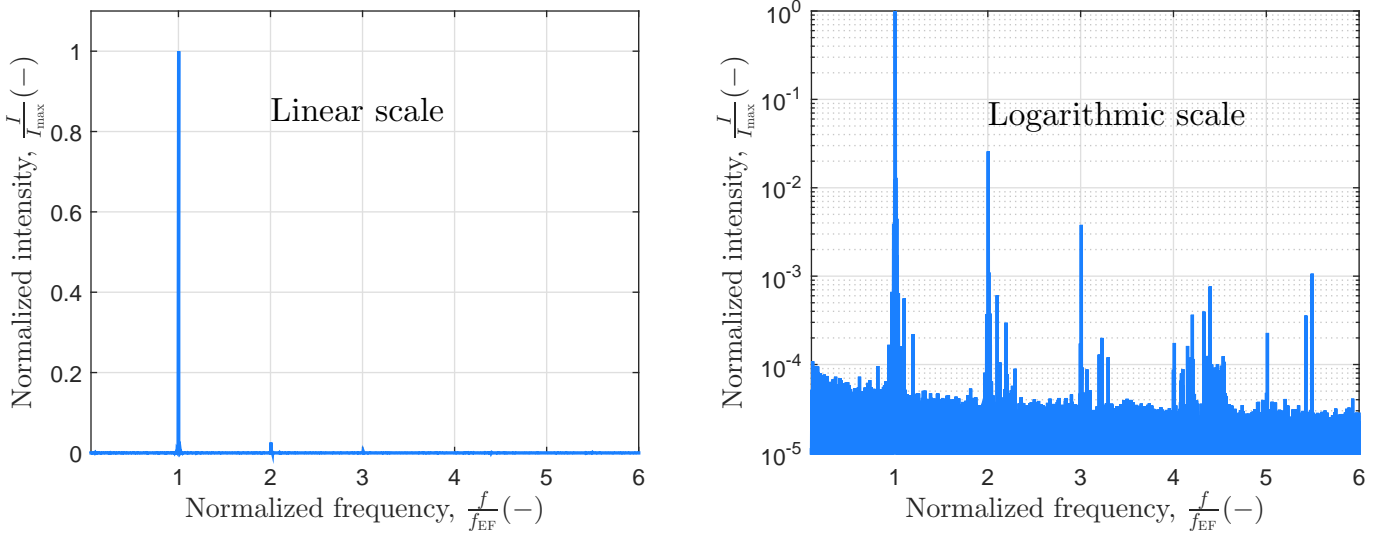


**Figure 15:** Experimentally measured beat spectrum for the rotating electro-optic quarter wave-plate described in figure 14. A flattop window has been applied to obtain a maximum FFT amplitude accuracy.<sup>24</sup> The left graph shows the spectrum on a linear scale, while the right graph uses a log-scale to further investigate the various sidebands. The experimental data displays a sideband efficiency of  $\eta_{\text{eo,qwp}} = 97.1\%$ . Optical power in other frequency bins is also observed due to setup maladjustments, as listed in table I.

## IX. Experimental results: Heterodyne displacement interferometry

### Heterodyne displacement interferometer; electro-optically generated split frequency

In this section the electro-optic rotating quarter wave-plate is implemented as a split-frequency generator in a heterodyne displacement interferometer. A 20kHz split frequency is generated by the rotating electro-optic quarter wave-plate, discussed in section VI. An overview of the heterodyne setup, including the electro-optic modulator, is shown in figure 16. A 1DOF precision-stage is used as a target, moving at a velocity of 1mm/s towards the optical beam. Both frequency paths are spatially separated to minimize periodic non-linearity due to frequency-separation. The reference- and measurement signals are fed into a lock-in amplifier (LIA) to determine the target's displacement. An overview of the most important components used in the setup is represented in table II. Experimental results of the electro-optic heterodyne interferometer are shown in figure 17.

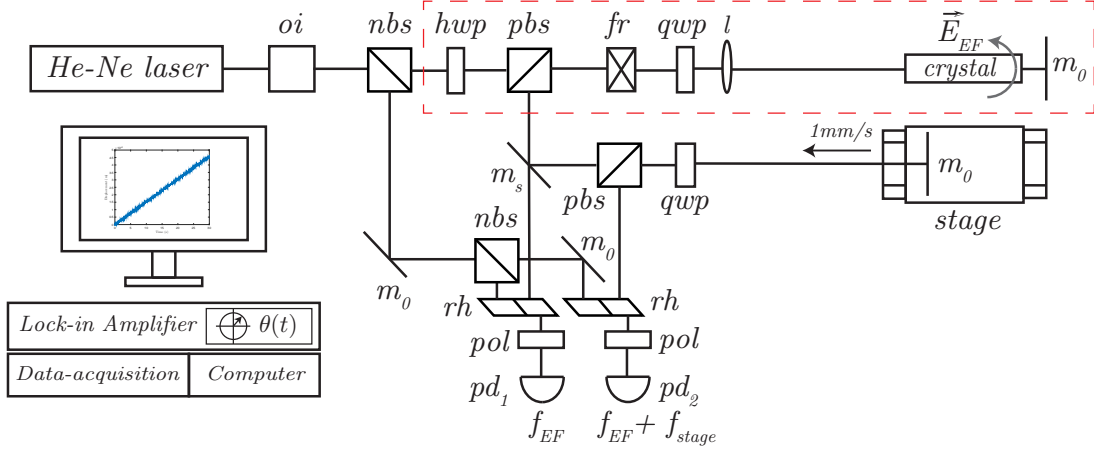


**Figure 16:** Schematic overview of the heterodyne displacement interferometer including the electro-optic rotating QWP, driven at a frequency  $f_{EF} = 20\text{kHz}$ . The red dashed box indicates the components involved in the frequency-shifting process. Both frequency paths are spatially separated to minimize frequency-separation periodic non-linearity. A reference beat signal is present on  $pd_1$ , while the second photo-detector  $pd_2$  creates the measurement signal. Both signals are fed into a lock-in amplifier to obtain the displacement data by phase-measurement. For a 1mm/s stage velocity,  $f_{stage} = 3.16\text{kHz}$   
*Legend:* *oi*; optical isolator, *nbs*; neutral beam-splitter, *hwp*; half wave-plate, *pbs*; polarizing beam-splitter, *fr*; Faraday rotator, *l*; lens, *qwp*; quarter wave-plate, *crystal*; *c-cut lithium niobate rod*, *m\_0*; mirror, *m\_s*; partial reflective mirror, *pol*; polarizer, *rh*; rhomboid, *pd*; photo-detector

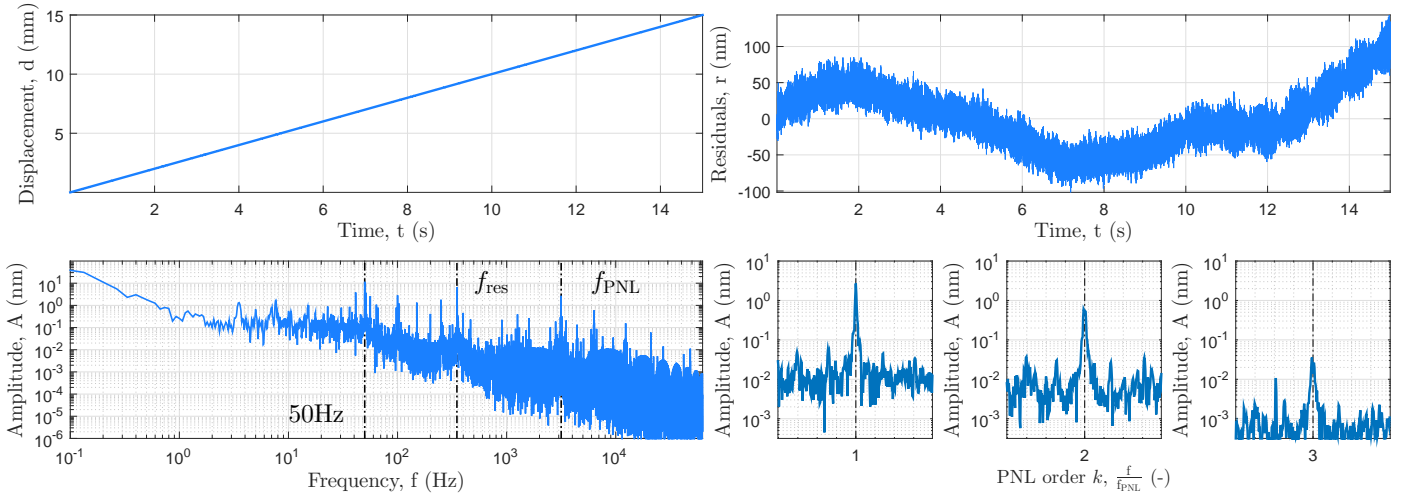


**Figure 17:** Experimental results of the electro-optic heterodyne displacement interferometer. The first subfigure shows the measured displacement as a function of time, while the second figure displays the periodic errors after subtracting the linear component. The frequency spectrum of these periodic errors displays various PNL orders, as shown in the graphic. Moreover, a low-frequent error is present due to air-flow in the environment, furthermore a 50Hz (accompanied by integer multiples) electro-magnetic interference signal and an optical component mechanical resonance  $f_{res}$  can be distinguished. Measurement time  $t = 15\text{s}$ , Sampling frequency  $f_s = 125\text{kHz}$ ,  $f_{PNL} = 3.16\text{kHz}$ ,  $N = 2$ ,  $\lambda = 633\text{nm}$ ,  $v_{stage} = 1\text{mm/s}$

### Heterodyne displacement interferometer; acousto-optically generated split frequency

A similar heterodyne displacement measurement, as described in the previous section, is performed by means of a commonly used split-frequency generator; an acousto-optic modulator. Figure 18 schematically displays this experimental setup. The acousto-optic modulators have a drive frequency  $f_1 = 39\text{MHz}$  and  $f_2 = 41\text{MHz}$  respectively, resulting in a  $2\text{MHz}$  split-frequency. By applying two frequency mixers, an external frequency generator and a low-pass filter, this  $2\text{MHz}$  split-frequency is mixed-down to  $20\text{kHz}$ , which is equal to the split-frequency generated by the electro-optic rotating quarter wave-plate in the previous section. Similarly the lock-in amplifier, in combination with the data-acquisition board, is used to determine the target displacement. Figure 19 shows the obtained experimental results.

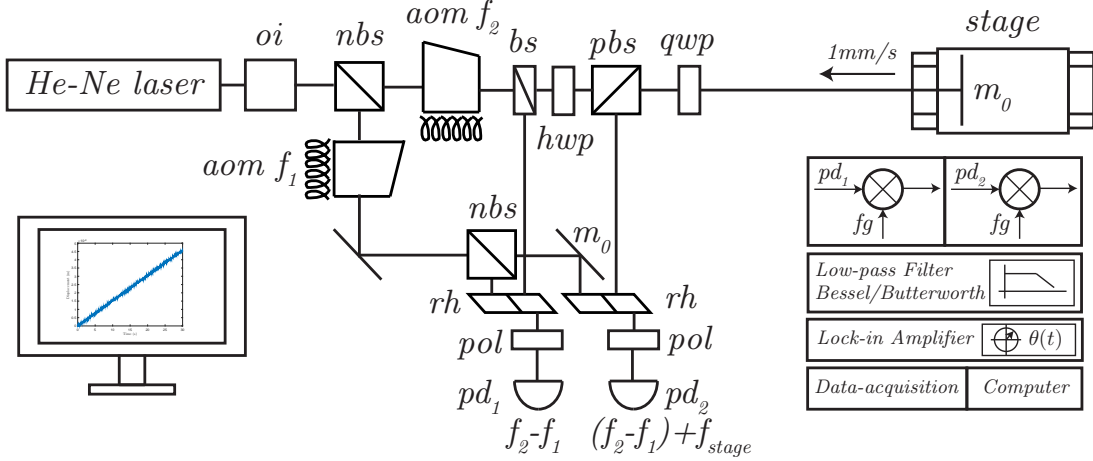


**Figure 18:** Schematic overview of the heterodyne displacement interferometer, including the acousto-optic modulators. The AOMs are driven at a frequency  $f_1 = 39\text{MHz}$  and  $f_2 = 41\text{MHz}$  respectively. The two frequency paths are spatially separated to minimize frequency-separation periodic non-linearity. A reference beat signal is present on  $pd_1$ , while the second photo-detector  $pd_2$  creates the measurement signal. These signals are fed into two frequency mixers and a low-pass filter to mix-down the frequency to  $20\text{kHz}$ , after which the lock-in amplifier is used to obtain the displacement data by phase measurement. For a  $1\text{mm/s}$  stage velocity,  $f_{\text{stage}} = 3.16\text{kHz}$

Legend: *oi*; optical isolator, *nbs*; neutral beam-splitter, *aom*; acousto-optic modulator, *bs*; beam-sampler, *hwp*; half wave-plate, *pbs*; polarizing beam-splitter, *qwp*; quarter wave-plate,  $m_0$ ; mirror, *pol*; polarizer, *rh*; rhomboid, *pd*; photo-detector

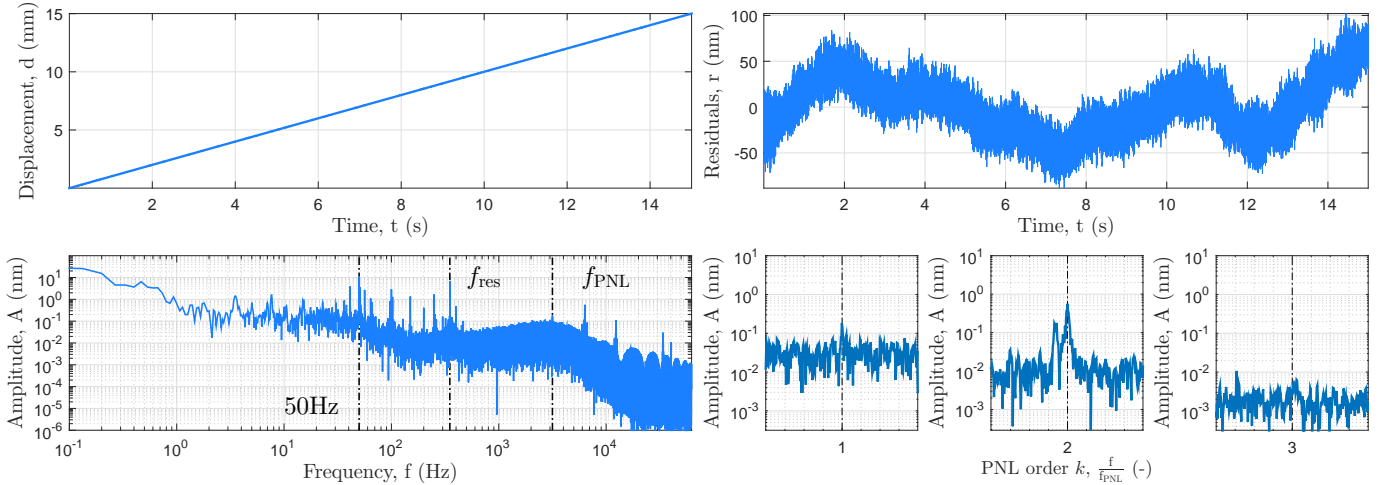


**Figure 19:** Experimental results of the acousto-optic heterodyne displacement interferometer. The first subfigure shows the measured displacement as a function of time, while the second figure displays the periodic errors after subtracting the linear component. The frequency spectrum of these periodic errors displays various PNL orders, as shown in the graphic. Moreover, a low-frequency error is present due to air-flow in the environment, furthermore a  $50\text{Hz}$  (accompanied by integer multiples) electro-magnetic interference signal and an optical component mechanical resonance  $f_{\text{res}}$  can be distinguished. Measurement time  $t = 15\text{s}$ , Sampling frequency  $f_s = 125\text{kHz}$ ,  $f_{\text{PNL}} = 3.16\text{kHz}$ ,  $N = 2$ ,  $\lambda = 633\text{nm}$ ,  $v_{\text{stage}} = 1\text{mm/s}$

### Heterodyne displacement interferometer; Zeeman-laser generated split-frequency

In this subsection a heterodyne displacement measurement is performed utilizing a Zeeman-laser to generate the split-frequency. The Zeeman-laser outputs a coaxial optical beam containing two mutually orthogonal polarized beams, which differ in frequency by 3.69MHz. A commercially available optical monolith is applied in this setup, in which the light travels to the target twice, enhancing measurement resolution, while doubling the PNL-frequency ( $N = 4$ ). Once more, two frequency mixers, an external frequency generator and a low-pass filter are used to mix-down the split-frequency to a 20kHz beat-signal. An overview of the experimental setup and experimental results are shown in figures 20 and 21 respectively.

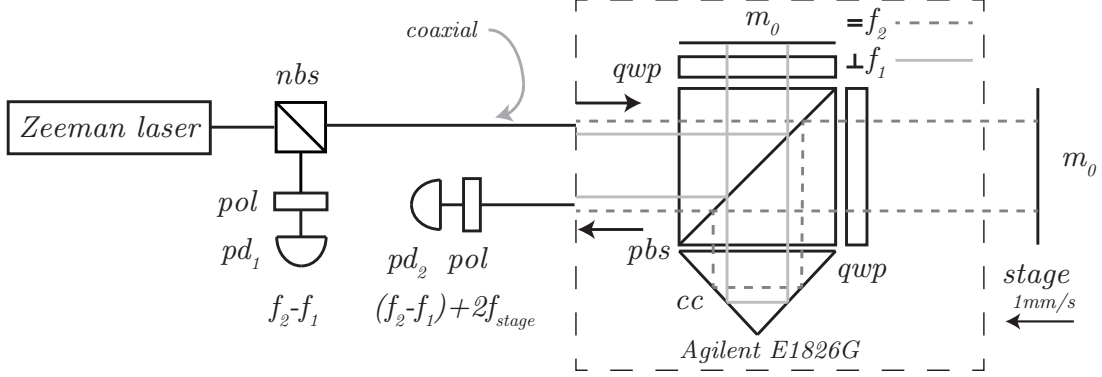


**Figure 20:** Schematic overview of the heterodyne displacement interferometer including a 3.69MHz Zeeman-laser and the Agilent E1826G optical monolith. The coaxial beam is splitted by a neutral beam-splitter, creating a reference beat signal on the first photodetector  $pd_1$ . The remaining coaxial optical beam travels into the optical monolith, after which it is incident on the second photo-detector  $pd_2$ . A fold factor of  $N = 4$  is present, as the optical beam travels to the target twice. Both signals are fed into two frequency mixers and a low-pass filter to mix-down the frequency to 20kHz, after which the lock-in amplifier is used to obtain the displacement data by phase-measurement. For a 1mm/s stage velocity,  $f_{stage} = 3.16\text{kHz}$

Legend: *nbs*; neutral beam splitter, *Agilent HI*; commercial heterodyne interferometer, *qwp*; quarter wave-plate, *m<sub>0</sub>*; mirror, *pol*; polarizer, *pd*; photo-detector

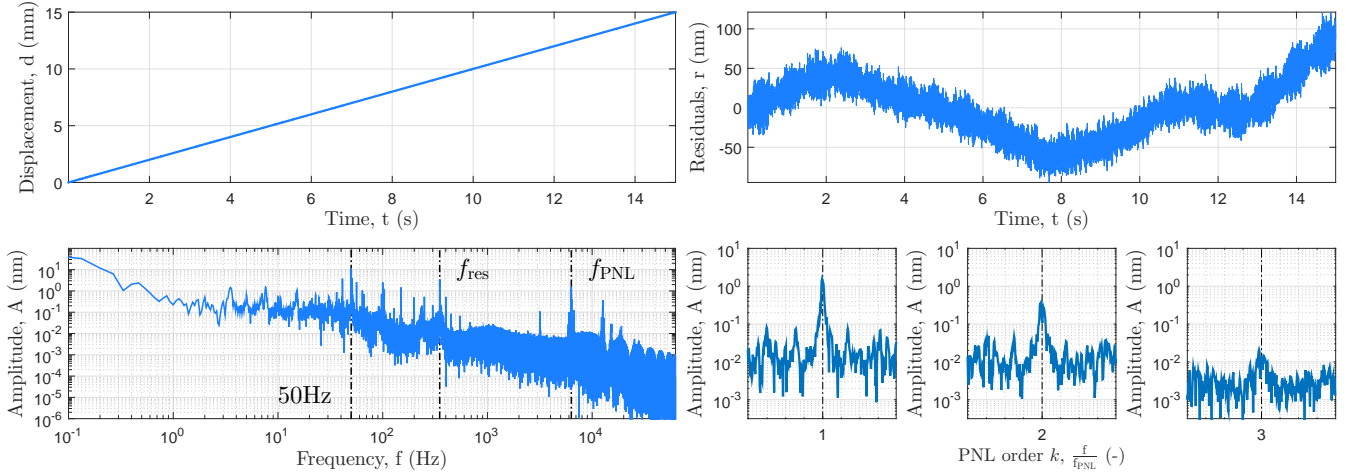


**Figure 21:** Experimental results of the heterodyne displacement interferometer, including a 3.69MHz Zeeman-laser as a split-frequency generator. The first subfigure shows the measured displacement as a function of time, while the second figure displays the periodic errors after subtracting the linear component. The frequency spectrum of these periodic errors displays various PNL orders, as shown in the graphic. Moreover, a low-frequent error is present due to air-flow in the environment, furthermore a 50Hz (accompanied by integer multiples) electro-magnetic interference signal and an optical component mechanical resonance  $f_{res}$  can be distinguished.

Measurement time  $t = 15\text{s}$ , Sampling frequency  $f_s = 125\text{kHz}$ ,  $f_{PNL} = 6.32\text{kHz}$ ,  $N = 4$ ,  $\lambda = 633\text{nm}$ ,  $v_{stage} = 1\text{mm/s}$

### Experimental results; an overview

Based on the experiments described in the previous sections, a quantitative comparison between the various split-frequency generators is made in terms of periodic non-linearity. From the residual frequency spectrum in figures 17, 19 and 21, the most dominant error sources were determined. Low-frequent errors are present as a result of air-flow between the different paths in the interferometers, leading to refractive index variations that account for phase-differences and are therefore interpreted as a displacement. Furthermore, a 50Hz component, accompanied by integer multiples, is present due to electro-magnetic interference from the electrical grid. In addition, the mechanical resonance frequency of an optical component in the setup is present as a periodic error. The influence of all these error sources can be reduced significantly by taking the proper measures. For instance, the errors regarding air-flow can be reduced by placing the interferometer in a vacuum environment. Shielding the measurement setup from electro-magnetic interference decreases the 50Hz (and multiples) error value drastically. However, the error resulting from periodic non-linearity is inherent to the measurement system, due to unwanted frequency-mixing as a result of e.g. alignment and polarization. An overview of these PNL-values for each measurement setup is shown in table III. From these results, it can be derived that the Zeeman-laser split-frequency generator shows a first-order PNL of 1.6nm. This value is primarily present due to frequency leakage during the separation process in the optical monolith. By using the acousto-optic modulators in combination with separated frequency paths, the first-order PNL can be reduced to 0.18nm, resulting from ghost-reflections inside the heterodyne interferometer. The electro-optic split-frequency generator inherits a first-order PNL of 2.7nm, mainly as a result from a polarization modulated carrier-frequency that leaks into the frequency-path traveling to the stage. Due to the low-pass filtering procedure inside the lock-in amplifier, higher sidebands were attenuated drastically and are therefore not present in the residual frequency spectrum.

**Table III:** Overview of the experimental results regarding non-linear periodic errors. The split-frequency is indicated by  $f_{\text{split}}$ , while  $k$  indicates the PNL-order. A schematic overview of the experimental setups is shown in figures 16, 18 and 20.

Measurement setup (split-frequency generator)	$f_{\text{split}}$ (MHz)	PNL value (nm)		
		$k = 1$	$k = 2$	$k = 3$
Electro-optic rotating QWP	0.020	2.7	0.59	0.036
Acousto-Optic Modulators	2.0	0.18	0.56	N.A.
Zeeman-laser	3.7	1.6	0.37	0.021

### X. Discussion & Conclusion

This research has demonstrated the implementation of a rotating electro-optic quarter wave-plate as a new means of split-frequency generator for heterodyne displacement interferometry. The split-frequency generator presented in this publication has advantages with respect to current state-of-the-art split-frequency generators, such as acousto-optic modulators and Zeeman-lasers. E.g., the electro-optic wave-plate can operate over a wide range of frequencies, ranging from several Hz to many MHz. Moreover, the operating frequency can be electrically adjusted and optical power is preserved, independent of the driving frequency. The displacement results obtained with the rotating electro-optic wave-plate were compared to current state-of-the-art split-frequency generators in terms of periodic non-linearity (PNL). Experimental results showed a first order PNL of 2.7nm for the electro-optic split-frequency generation, versus 1.6nm and 0.18nm for the ZL and AOM respectively. Moreover, experiments have been performed to determine the sideband efficiencies of both mechanically and electro-optic rotating wave-plates. The mechanically rotating half- and quarter wave-plate showed sideband efficiencies of  $\eta_{\text{me,hwp}} = 99.1\%$  and  $\eta_{\text{me,qwp}} = 99.2\%$  respectively. Whereas the electro-optic rotating quarter wave-plate exhibits a sideband efficiency of  $\eta_{\text{eo,qwp}} = 97.1\%$

#### Future Improvements

The first-order PNL value for the heterodyne displacement interferometer, which utilizes an electro-optic generated split-frequency, can be further reduced by optimizing the performance of the modulator to prevent any carrier-frequency leaking into the optical path towards the target. Furthermore, in order for the electro-optic rotating wave-plate to be implemented in interferometers that measure high target-velocities (several meters per second), the split frequency should be increased (multiple MHz), relative to what this publication showed as a proof of concept (20kHz). However, by increasing the driving frequency, the crystal absorbs a large amount of power, which deteriorates the performance of the modulator. Either a heat-sink should be added in the setup, or the quarter-wave voltage has to be decreased by producing crystals with a larger aspect ratio. By creating an 8-electrode setup surrounding the crystal, illustrated in figure 6f, thinner crystals can be used as the homogeneous electric-field area is increased significantly. Other possibilities emerge in the field of photonics. By producing an on-chip lithium niobate wave-guide, modulation frequencies in the order of GHz can be achieved.<sup>37</sup>

#### Future Applications

The application of the described modulator in a heterodyne displacement interferometer promises to introduce a new method of heterodyne detection. Currently, using a static split-frequency, a phase-measurement board or lock-in amplifier is used to determine the target-displacement. By using a tunable rotating electro-optic wave-plate, one could try to retain a static beat-frequency at the phase-board, while adjusting the split-frequency

using an analog feedback-loop. Applying this technique, the information regarding the target's displacement is contained in the modulator's electric-field driving frequency.

When using a linear input polarization, the described modulator could be used to create a coaxial optical beam, similar to the Zeeman-laser. In contrast to the Zeeman-laser, the electro-optic modulator's split-frequency can be increased without losing any optical power. This process is described by the single-pass operation in section two and three. Additionally, the modulator can be applied to generate tunable hyper-fine frequency combs by utilizing an electro-optic modulator ring<sup>38,39</sup> or by placing the modulator inside a high-Q optical cavity.

## References

- <sup>1</sup>Norman Bobroff. Recent advances in displacement measuring interferometry. *Measurement Science and Technology*, 4(9):907, 1993.
- <sup>2</sup>Frank C Demarest. High-resolution, high-speed, low data age uncertainty, heterodyne displacement measuring interferometer electronics. *Measurement Science and Technology*, 9(7):1024, 1998.
- <sup>3</sup>Alex Abramovici, William E Althouse, Ronald WP Drever, Yekta Gürsel, Seiji Kawamura, Frederick J Raab, David Shoemaker, Lisa Sievers, Robert E Spero, Kip S Thorne, et al. Ligo: The laser interferometer gravitational-wave observatory. *Science*, 256(5055):325–333, 1992.
- <sup>4</sup>Karsten Danzmann, LISA Study Team, et al. Lisa: laser interferometer space antenna for gravitational wave measurements. *Classical and Quantum Gravity*, 13(11A):A247, 1996.
- <sup>5</sup>Thilo Schuldt, Martin Gohlke, Dennis Weise, Ulrich Johann, Achim Peters, and Claus Braxmaier. Picometer and nanoradian optical heterodyne interferometry for translation and tilt metrology of the lisa gravitational reference sensor. *Classical and Quantum Gravity*, 26(8):085008, 2009.
- <sup>6</sup>Jonathan Leach, Miles J Padgett, Stephen M Barnett, Sonja Franke-Arnold, and Johannes Courtial. Measuring the orbital angular momentum of a single photon. *Physical review letters*, 88(25):257901, 2002.
- <sup>7</sup>Adrianus Korpel. Acousto-optics a review of fundamentals. *Proceedings of the IEEE*, 69(1):48–53, 1981.
- <sup>8</sup>H Takasaki, N Umeda, and M Tsukiji. Stabilized transverse zeeman laser as a new light source for optical measurement. *Applied optics*, 19(3):435–441, 1980.
- <sup>9</sup>T Maekawa, T Minami, K Makino, S Tanaka, S Kubo, and M Iguchi. Frequency shift of 1.45 mhz for 337- $\mu$ m hcn laser beam with a super rotating grating. *Review of scientific instruments*, 62(2):304–307, 1991.
- <sup>10</sup>Warren H Stevenson. Optical frequency shifting by means of a rotating diffraction grating. *Applied Optics*, 9(3):649–652, 1970.
- <sup>11</sup>PJ Allen. A radiation torque experiment. *Am. J. Phys*, 34(12):1185–1192, 1966.
- <sup>12</sup>Bruce A Garetz and Stephen Arnold. Variable frequency shifting of circularly polarized laser radiation via a rotating half-wave retardation plate. *Optics Communications*, 31(1):1–3, 1979.
- <sup>13</sup>R Simon, HJ Kimble, and ECG Sudarshan. Evolving geometric phase and its dynamical manifestation as a frequency shift: an optical experiment. *Physical review letters*, 61(1):19–22, 1988.
- <sup>14</sup>Mahendra P Kothiyal and Claude Delisle. Optical frequency shifter for heterodyne interferometry using counterrotating wave plates. *Optics letters*, 9(8):319–321, 1984.
- <sup>15</sup>Yao Li and George Eichmann. Multipass counterrotating waveplate frequency shifters for heterodyne interferometry. *Optics letters*, 11(11):718–720, 1986.
- <sup>16</sup>Richard N Shagam and James C Wyant. Optical frequency shifter for heterodyne interferometers using multiple rotating polarization retarders. *Appl. Opt*, 17:3034–3035, 1978.
- <sup>17</sup>CF Buhner, D Baird, and EM Conwell. Optical frequency shifting by electro-optic effect. *Applied Physics Letters*, 1(2):46–49, 1962.
- <sup>18</sup>J Campbell and William H Steier. Rotating-waveplate optical-frequency shifting in lithium niobate. *Quantum Electronics, IEEE Journal of*, 7(9):450–457, 1971.
- <sup>19</sup>Gary E Sommargren. Up/down frequency shifter for optical heterodyne interferometry. *JOSA*, 65(8):960–961, 1975.
- <sup>20</sup>Arjan JH Meskers, Jo W Spronck, and Robert H Munnig Schmidt. Heterodyne displacement interferometer, insensitive for input polarization. *Optics letters*, 39(7):1949–1952, 2014.
- <sup>21</sup>JH Poynting. On pressure perpendicular to the shear planes in finite pure shears, and on the lengthening of loaded wires when twisted. *Proceedings of the Royal Society of London. Series A, Containing Papers of a Mathematical and Physical Character*, 82(557):546–559, 1909.
- <sup>22</sup>Bruce A Garetz. Angular doppler effect. *JOSA*, 71(5):609–611, 1981.
- <sup>23</sup>R Clark Jones. A new calculus for the treatment of optical systems. *JOSA*, 31(7):488–493, 1941.
- <sup>24</sup>Robert W. Ramirez. *The FFT, Fundamentals and Concepts*. Prentice-Hall, New Jersey, USA, 1985.
- <sup>25</sup>RS Weis and TK Gaylord. Lithium niobate: summary of physical properties and crystal structure. *Applied Physics A*, 37(4):191–203, 1985.
- <sup>26</sup>IP Kaminow and EH Turner. Electrooptic light modulators. *Applied optics*, 5(10):1612–1628, 1966.
- <sup>27</sup>AW Warner, M Onoe, and GA Coquin. Determination of elastic and piezoelectric constants for crystals in class (3m). *The journal of the acoustical society of America*, 42(6):1223–1231, 1967.
- <sup>28</sup>IP Kaminow. Barium titanate light modulator. ii. *Applied Physics Letters*, 8(11):305–307, 1966.
- <sup>29</sup>EG Spencer, PV Lenzo, and K Nassau. Elastic wave propagation in lithium niobate. *Applied Physics Letters*, 7(3):67–69, 1965.
- <sup>30</sup>S. Wang. *Solid state electronics*. McGraw Hill Book Co., New York, USA, 1966.
- <sup>31</sup>J.T. Milek and M. Neuberger. *Linear Electrooptic Modular Materials*. Plenum Publishing Corporation, New York, USA, 1972.
- <sup>32</sup>MV Hobden and J Warner. The temperature dependence of the refractive indices of pure lithium niobate. *Physics Letters*, 22(3):243–244, 1966.
- <sup>33</sup>JD Zook, D Chen, and GN Otto. Temperature dependence and model of the electro-optic effect in linbo3. *Applied Physics Letters*, 11(5):159–161, 1967.
- <sup>34</sup>Chien-ming Wu. Periodic nonlinearity resulting from ghost reflections in heterodyne interferometry. *Optics communications*, 215(1):17–23, 2003.
- <sup>35</sup>SJAG Cosijns, Han Haitjema, and PHJ Schellekens. Modeling and verifying non-linearities in heterodyne displacement interferometry. *Precision Engineering*, 26(4):448–455, 2002.
- <sup>36</sup>A.J.H. Meskers. *On the improvement of heterodyne displacement interferometry*. <http://respository.tudelft.nl>, Delft, The Netherlands, 2014.
- <sup>37</sup>Reinhold Noe and DA Smith. Integrated-optic rotating waveplate frequency shifter. *Electronics Letters*, 24(21):1348–1349, 1988.
- <sup>38</sup>Poul Jessen and Martin Kristensen. Generation of a frequency comb with a double acousto-optic modulator ring. *Applied optics*, 31(24):4911–4913, 1992.
- <sup>39</sup>Han Young Ryu, Han Seb Moon, and Ho Suhng Suh. Optical frequency comb generator based on actively mode-locked fiber ring laser using an acousto-optic modulator with injection-seeding. *Optics express*, 15(18):11396–11401, 2007.



# 2

## APPENDIX



## AEROTECH 1DOF PRECISION-STAGE (ABL1000 SERIES)

Measurements performed during this research, utilized the Aerotech precision-stage as a target. This stage has very good specifications with respect to resolution, accuracy and repeatability. The ABL1000 series support travel ranges of over 100mm. A table of the most important specs is shown in figure 2.1

Basic Model		ABL1000			
Total Travel		25 mm (1in)	50 mm (2in)	100 mm (4in)	150 mm (6in)
Drive System		Linear Brushless Servomotor			
Feedback		Noncontact Linear Encoder (LN or LT)			
Resolution	LN	0.5 nm (0.04 µin)			
	LT	2.5 nm (0.2 µin)			
Maximum Travel Speed <sup>(1)</sup>		300 mm/s (12 in/s)			
Maximum Load <sup>(2)</sup>		15.0 kg (33.0 lb)			
Overall Accuracy	LN <sup>(1)</sup>	±0.2 µm (±8 µin) <sup>(3)</sup> ; ±1 µm (±40 µin)	±0.2 µm (±8 µin) <sup>(3)</sup> ; ±1 µm (±40 µin)	±0.2 µm (±8 µin) <sup>(3)</sup> ; ±2 µm (±80 µin)	±0.5 µm (±20 µin) <sup>(3)</sup> ; ±5 µm (±200 µin)
	LT <sup>(2)</sup>	±0.3 µm (±12 µin) <sup>(3)</sup> ; ±2 µm (±80 µin)	±0.3 µm (±12 µin) <sup>(3)</sup> ; ±2 µm (±80 µin)	±0.3 µm (±12 µin) <sup>(3)</sup> ; ±5 µm (±200 µin)	±0.5 µm (±20 µin) <sup>(3)</sup> ; ±5 µm (±200 µin)
Repeatability	LN <sup>(3)</sup>	±50 nm (±2 µin)			
	LT <sup>(3)</sup>	±50 nm (±2 µin) <sup>(3)</sup> ; ±100 nm (±4 µin)			

Figure 2.1: ABL1000 series specs

The stage can be controlled by means of a script written in the 'Soloist motion composer' software. This software is installed on the desktop computer (Service Tag: DLPG85J, Asset Number: TUD203130) in the Optics Lab. In order to control the stage, some steps have to be followed with respect to the connection and operation, these will briefly be listed below.

1) You can connect to the stage by plugging in the network cable that runs from the motor controller (below the Thorlabs vibration isolation table) to the network card of the desktop, please use the port that connects directly to the motherboard. Do not forget to remove the cable that connects to the TU-Delft network, this cable is labeled as 'TU Delft'.

2) When you have established a connection, startup the 'Soloist Motion Composer' software. This can be done via the steps shown below. After starting the program, you should see screen as displayed in the picture.

Start ⇒ All programs ⇒ Aerotech ⇒ Soloist ⇒ Soloist Motion Composer

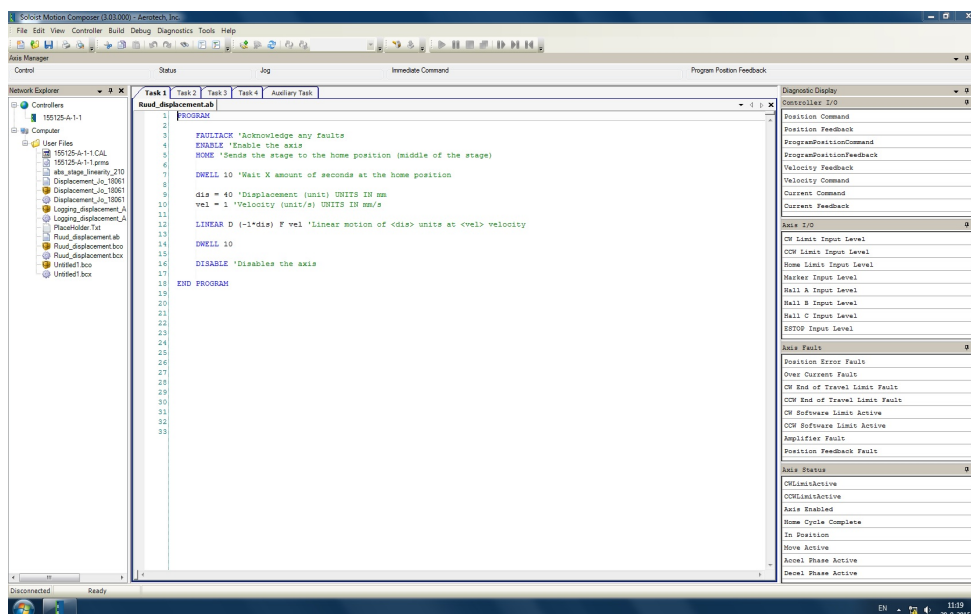


Figure 2.2: Soloist Motion Composer startup screen

Now you can connect to the controller by clicking on 'Connect' in the 'Controller' tab. This should give you the screen shown in the figure below, where you can already control the stage manually after pressing 'Enable'. For instance, try a homing procedure by pressing the home button. Now you should see the stage moving back and forth.

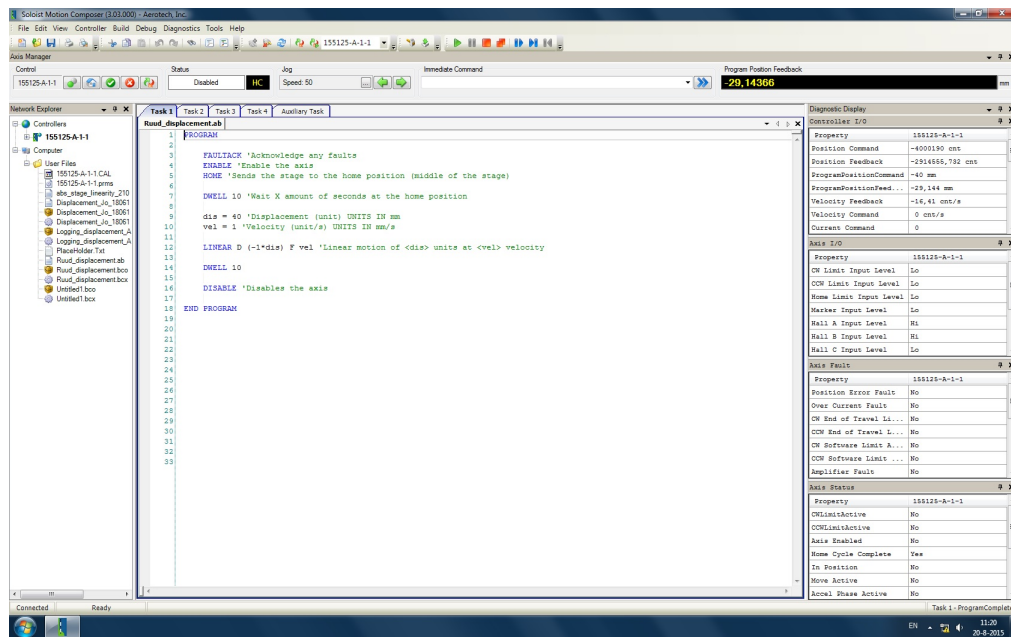


Figure 2.3: Soloist Motion Composer screen when a connection is established

3) The trajectory of the stage can be programmed by writing some code into the editor. To make your life a little easier, some code has been written that represents the most used trajectories. This includes:

- Linear displacement trajectory
- Incremental stepping motion

If you need a more exotic trajectory, with a certain velocity and displacement profile, please look into the 'Soloist Programming Help' file to write the proper script. The script is saved on the hard-disk as 'Trajectories.ab'. As this might be accidentally deleted or lost, a screenshot of this file is shown below. You can select the trajectory of interest, by commenting the other sections using the apostrophe key. By pressing the run command the script will be evaluated and the stage will move accordingly.

```

Trajectories.ab
1 PROGRAM
2
3     FAULTACK 'Acknowledge any faults
4     ENABLE 'Enable the axis
5     HOME 'Sends the stage to the home position (middle of the stage)
6
7     DWELL 10 'Wait X amount of seconds at the home position
8
9     'LINEAR DISPLACEMENT TRAJECTORY
10    dis = 10 'Displacement (unit) units in mm
11    vel = 1 'Velocity (unit/s) units in mm/s
12
13    LINEAR D (-1*dis) F vel 'Linear motion of <dis> units at <vel> velocity
14
15    'STEPPING MOTION
16    stp = 1 'Displacement per step UNITS in mm/s
17    vel = 1 'Velocity of that described trajectory
18
19    REPEAT 10 'Execute the described motion 'X' times*6
20        MOVEINC D -1*stp F vel 'Move incremental steps
21        DWELL 1 'Wait between the different steps (seconds)
22    END REPEAT
23
24    DWELL 10
25
26    DISABLE 'Disables the axis
27
28 END PROGRAM

```

Figure 2.4: Code for a linear- or incremental displacement trajectory

---

## AGILENT N1225A HIGH RESOLUTION LASER AXIS BOARD

The N1225A axis board is a phase-measurement board with four optical channels that can support a three-axis laser measuring system. In this research it was predominantly used as part of a heterodyne displacement interferometer, to determine the displacement of a 1DOF stage. This practical guide will quickly guide you through some crucial steps in order to properly implement this board into your measurement setup.

### DATA READOUT

The data w.r.t. the calculated phase can be read directly from the measurement board. In this configuration the board acts as the server, while you are the client. Therefore, we have to connect to the board using a LAN-connection. An ethernet port is located at the front-panel of the board, connect your computer to this port through an ethernet cable. Please follow the upcoming steps in order to read-out the data.

1) In order to communicate to the server, it is most convenient to set-up your LAN-connection using a static IP address. This can be done by adapting your TCP/IP settings. You can easily check your LAN-settings using the command prompt by typing: `ipconfig /all`

Start ⇒ Control Panel ⇒ Network & Sharing Center ⇒ Change adapter settings ⇒ Local Area Connection - Change settings of this connection ⇒ Internet Protocol v4 (TCP/IPv4) - Properties

---

You can get IP settings assigned automatically if your network supports this capability. Otherwise, you need to ask your network administrator for the appropriate IP settings.

Obtain an IP address automatically

Use the following IP address:

IP address:	192 . 168 . 111 . 11
Subnet mask:	255 . 255 . 255 . 0
Default gateway:	192 . 168 . 111 . 1

Figure 2.5: Setting a static IP address to read-out the data. Make sure your IP address does not coincide with another device! If it does, choose any other which uses the same subnet mask.

2) Now that you've set your static-IP, you can easily communicate with the server by means of your internet browser. The IP-address of the measurement board is shown below.

IP-address : 192.168.111.10

When you are connected to the board through your LAN connection, enter the IP-address into your browser's URL section, which should bring you to the page shown in figure 2.6. This page basically tells you all the information about the board, such as the MAC- and IP-address

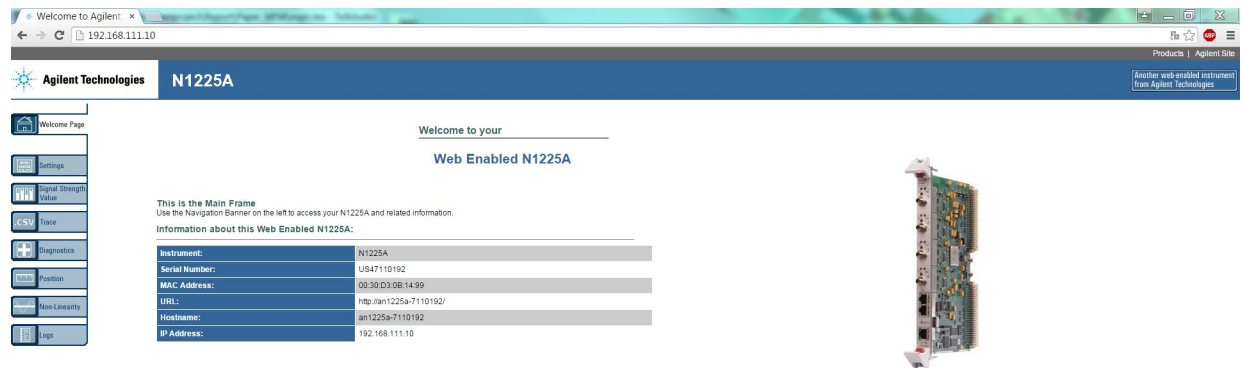


Figure 2.6: Agilent N1225A homepage

From this page you can set-up your measurement read-out, as well as managing the board's settings. You can visit the 'Settings' section to change the LAN-settings of the phase-board, to avoid problems, please keep them as they are. Information about the firmware can also be found here.

#### N1225A LAN Settings

MAC Address:	00:30:D3:0B:14:99
Serial Number:	US47110192
URL:	http://an1225a-7110192/
Hostname:	<input type="text" value="an1225a-7110192"/>
Domain Name:	<input type="text"/>
IP Address:	<input type="text" value="192.168.111.10"/>
Netmask:	<input type="text" value="255.255.255.0"/>
Default Gateway:	<input type="text" value="192.168.111.1"/>
DHCP:	<input type="radio"/> On <input checked="" type="radio"/> Off

Figure 2.7: Agilent N1225A LAN-settings

#### N1225A Firmware

Software Version:	B.37
Hardware Version:	B.02
FPGA Version:	4276
Options:	200
Upgrade Firmware:	<input type="button" value="Upgrade"/>

Figure 2.8: Agilent N1225A firmware versions

Information about the diagnostics of the device can be acquired through the diagnostics tab. Please make sure the temperature of the various channels does not reach excessive levels.

**Always make sure the fan is turned on while you are using the board!**

#### In Service Diagnostic Tests

FPGA Programmed:	Yes
DIP Switch Position:	S3: 00000000 S2: 01000011 S1: 00000111
Channel Temperature:	1 is 27 degC 2 is 28 degC 3 is 27 degC 4 is 27 degC
Power Supplies:	+1.2V PASSED +2.5V PASSED +3.3V [3.29V] PASSED +12.0V [12.02V] PASSED -12.0V [-11.75V] PASSED +50.0V [50.98V] PASSED
SPI EEPROM Test:	PASSED
Internal Comm Bus Test:	PASSED
Flash RAM Test:	PASSED
Loopback Ping:	PASSED
Network Ping:	<input type="text"/> <input type="button" value="Ping"/>
Out of Service Tests:	<input type="button" value="Execute"/>

Figure 2.9: Agilent N1225A firmware versions

You can visit the trace tab to set-up your measurement.

**Action:** Used to start (arm) and stop the measurement.

**Frequency divider:** Enter your divider, related to your sampling frequency. Five is the minimum, which indicates your maximum sampling frequency of 62.5kSa/s. Please do not forget to click 'update'.

**Output file:** You can download your CSV-file here, after your measurement has been completed.

**Status:** Status of the device. Ready to use when 'Idle', measurement running when 'Armed'.

On the Board Reset Control you can clear the errors, if any are present.

#### Trace Control

Action:	<input type="button" value="Arm"/> <input type="button" value="Stop"/>
312.5kHz Divider:	<input type="text" value="5"/> 62.5000 ksps <input type="button" value="Update"/>
Output File:	default
Status:	<input type="text" value="Idle"/>

#### Board Reset Control

Clear Errors:	<input type="button" value="Clear"/>
Axis 1:	<input type="text" value="0x0"/> <input type="button" value="Preset"/> <input type="checkbox"/> Reset position with preset value <input type="button" value="Reset"/>
Axis 2:	<input type="text" value="0x0"/> <input type="button" value="Preset"/> <input type="checkbox"/> Reset position with preset value <input type="button" value="Reset"/>
Axis 3:	<input type="text" value="0x0"/> <input type="button" value="Preset"/> <input type="checkbox"/> Reset position with preset value <input type="button" value="Reset"/>
Axis 4:	<input type="text" value="0x0"/> <input type="button" value="Preset"/> <input type="checkbox"/> Reset position with preset value <input type="button" value="Reset"/>

Figure 2.10: Agilent N1225A trace control

In the axis-setup subtab you will find your active measurement axes and your sampling frequency. Please enter the axis between which you want to measure, as well as the data you want to receive in your CSV file. The channels correspond to the channels on the front panel of the board. Again, do not forget to click 'update'.

#### Axis Setup

Rate:	62.5000 Ksps
Axis 1:	<input type="checkbox"/> Enable Data Recording <input type="checkbox"/> Direction Sense <input type="checkbox"/> Include Phase Measurement Source A Channel 1 ▼ Source B Channel 4 ▼
Axis 2:	<input type="checkbox"/> Enable Data Recording <input type="checkbox"/> Direction Sense <input type="checkbox"/> Include Phase Measurement Source A Channel 2 ▼ Source B Channel 4 ▼
Axis 3:	<input type="checkbox"/> Enable Data Recording <input type="checkbox"/> Direction Sense <input type="checkbox"/> Include Phase Measurement Source A Channel 3 ▼ Source B Channel 4 ▼
Axis 4:	<input type="checkbox"/> Enable Data Recording <input type="checkbox"/> Direction Sense <input type="checkbox"/> Include Phase Measurement Source A Channel 4 ▼ Source B Channel 4 ▼
Update	

Figure 2.11: Agilent N1225A measurement axis setup

In the trigger setup subtab you can set any triggers, relating to the various channels. For a further description please look into the user manual.

#### Trigger Setup

	/T4 /T3	/T2 /T1	/T2 T1	T2 /T1	T2 T1
Trigger Enable:	<input type="checkbox"/>	<input type="checkbox"/>	<input type="checkbox"/>	<input type="checkbox"/>	<input type="checkbox"/>
Trigger 1:	Axis: Axis 1 ▼ Source: Trigger Off ▼				
Trigger 2:	Axis: Axis 1 ▼ Source: Trigger Off ▼				
Trigger 3:	Axis: Axis 1 ▼ Source: Trigger Off ▼				
Trigger 4:	Axis: Axis 1 ▼ Source: Trigger Off ▼				
Update					

Figure 2.12: Agilent N1225A measurement axis setup

You can set-up the settings of your measurement output file in the CSV-file subtab. The name and heading

can be chosen, as well as the file formatting. Moreover provide your samples before/after trigger. If you do not want to trigger automatically, you can enter the maximum amount of samples before the trigger.

#### CSV File

Number of axes:	0
Samples before Trigger:	10920 Adjusted for number of axes, Max. Value: 699056
Samples after Trigger:	21840 Adjusted for number of axes
Test Name:	default
End-of-line:	<input checked="" type="radio"/> DOS (CR-LF) <input type="radio"/> Unix (CR)
Header:	<input type="checkbox"/> Include time of day <input type="checkbox"/> Include test name
Sample Unit:	<input checked="" type="radio"/> None <input type="radio"/> sample# <input type="radio"/> us <input type="radio"/> ms <input type="radio"/> s
Update	

Figure 2.13: Agilent N1225A measurement axis setup

Now you can start your measurement in the 'Trace Control' subtab by pressing the 'Arm' button. After which you can download the .csv file from the same subtab, right click to 'save as' to your preferred location.

### MEASUREMENT SETUP

The laser-axis board can be easily used in combination with the acousto-optic modulators (AOM) and the Zeeman-laser (ZL). Simply provide one channel with a reference beat signal, while another channel receives the measurement beat signal.

Error LED signal	Error
-	No error
Orange	AC-power too high
Orange	DC-power too high
Orange	Loss of lock condition (check interference)

Table 2.1: Overview of front-panel LED's and their error sources

Signal LED signal	Error
Green	Proper signal to perform a measurement
Flash	AC-power too high
Flash	DC-power too high
-	No interference detected

## LOCK-IN AMPLIFIER, FREQUENCY MIXERS AND LOW-PASS FILTER

To acquire the displacement data described in the main body of this report, a Lock-in Amplifier (LIA) was used in combination with two Frequency Mixers (FM) and a Low-pass Filter (LPF). This guide will shortly discuss some practical details on how to use these devices. There are excellent 'Getting started' sections in the user-manuals, therefore the working-principle of the devices is not discussed here.

### OBTAINING DISPLACEMENT DATA USING A LOCK-IN AMPLIFIER

Displacement data can be easily obtained using a Lock-in Amplifier. Please make sure you have a proper reference and measurement beat signal incident on your photo-detectors. The steps below will guide you through the process.

1) Turn on the Lock-in Amplifier and plug in your reference and measurement signals into the lock-in amplifier connectors. The measurement signal should be plugged into the A/I port in the Signal Input section. The reference signal can be plugged into the Ref port, after which the LIA will lock on this frequency. The figure below shows you an overview of where to plug-in your coaxial cables.

2) You should now set the proper settings in order to make your measurements. On the signal input, please enter the following settings.

Table 2.2: Various settings of the LIA to obtain displacement data

Setting	Value
Input	A
Couple	AC
Ground	Ground
Reserve	High reserve
Filters	Line & 2xLine

3) Now set the proper settings for your low-pass filter. You can set the time constant, which relates to the cut-off frequency as shown in the equation below. Moreover, you can set the filter's Roll-off slope. It is most convenient to set the roll-off to 24db/oct, to minimize the influence of higher sideband frequencies.

$$f_{co} = \frac{1}{2\pi\tau}$$

Where  $f_{co}$  is the cut-off frequency in Hertz, and  $\tau$  is the time-constant in seconds, which you can adjust on the LIA. It is advised to place your cut-off frequency, just above your Doppler-shift related to your target's velocity.

For instance, for a target moving at 1mm/s, the Doppler-shift equals 3159Hz. By setting the time constant  $\tau = 30\mu\text{s}$ , your cut-off frequency is equal to 5305Hz.

The sensitivity parameter serves as an amplifier, this will amplify your output value depending on the setting. Just try some setting, depending on your signal strengths. Please make sure you do not overload the LIA.

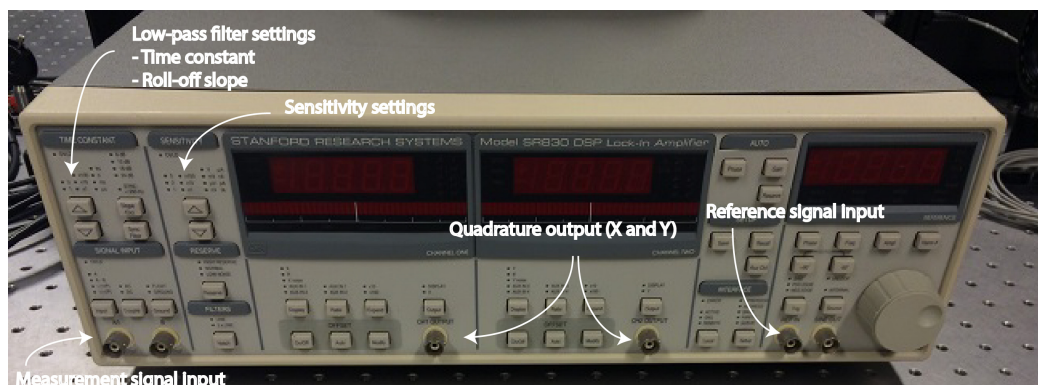


Figure 2.14: Photograph of the Lock-In Amplifier

---

4) By setting the output settings of the LIA to the X and Y value respectively, you will have a quadrature output vector. Where the length of the vector equals your voltage output amplitude, and the phase of the vector relates to the displacement traveled by your target.

$$V_{\text{sig}} = \sqrt{X^2 + Y^2} \quad \theta = \arctan\left(\frac{Y}{X}\right)$$

By acquiring both the X and the Y signal, which should represent a cosine and sine voltage respectively, you can easily determine the target displacement by unwrapping the phase  $\theta(t)$  using MATLAB or Python.

### MIXING DOWN YOUR SPLIT-FREQUENCY USING FREQUENCY MIXERS AND A LOW-PASS FILTER

As the 2MHz and 3.69MHz split-frequency generated by the acousto-optic modulators (AOM) and Zeeman-laser respectively inherit a frequency that is too high for the LIA, these should be mixed down to lower values. This can be easily done using two frequency mixers, an external frequency generator and a low-pass filter. By mixing two frequency together, you will obtain a signal that contains a superposition of the sum of the frequencies and the difference of the two frequencies. When passing these through a low-pass filter, you end up with only the low-frequent component. This is schematically shown in the figure below.

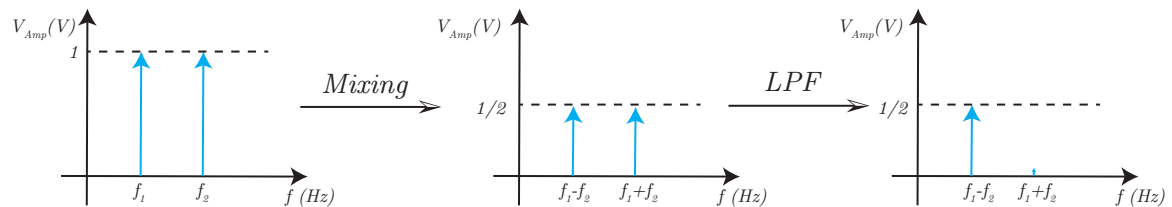


Figure 2.15: Mixing and Low-pass filter procedure

For example, if you mix the 2MHz output from the photo-detectors with a 2.02MHz signal generated by the frequency generator, this results in a 4.02MHz signal and a 20kHz signal. After a pass through a low-pass filter, with for instance a cutoff frequency  $f_{co} = 50\text{kHz}$ , only the 20kHz signal is present in your output. A picture of the frequency mixers and the low-pass filter is shown below. Including a schematic that shows you the inputs and outputs.

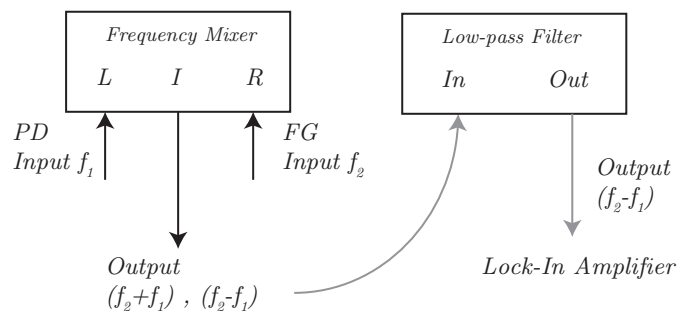


Figure 2.16: Mixing and Low-pass filter schematic



Figure 2.17: Photograph of the low-pass filter

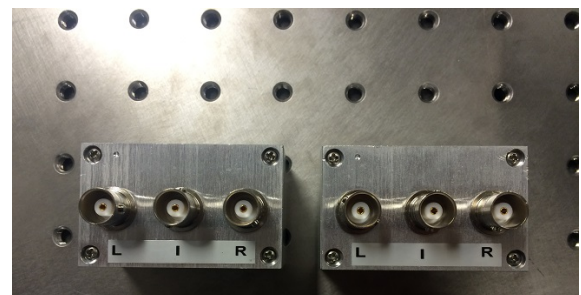


Figure 2.18: Photograph of the two frequency mixers

## NI-DAQ USB-6211 - DATA ACQUISITION

Acquiring data using the USB-6211 is a rather simple procedure, this guide shows you some simple tips and tricks to get started. Please make sure you have downloaded and installed the NI-DAQmx drivers (Black-board). The data can be easily acquired using either MATLAB or Labview, experience learns that MATLAB is most convenient to use. Table 2.3 displays an overview of the most important parameters regarding the USB-6211 w.r.t. reading out data from an analog signal.

- 1) As a first step, determine whether you want to measure differential (i.e. difference between two electrodes) or single ended (i.e. measurement between electrode and the device's ground).
- 2) Insert the electrodes in the device's ports. Please make sure you connect them properly and use figure 2.19 as a guide. As an example, if you want to measure differential on channel AI0, insert the electrodes in ports 15 (AI0) and 16 (AI8) respectively.
- 3) Insert the USB-cable into your computer and startup MATLAB. Your computer will notify the device has been detected and the LED on the device starts blinking.
- 4) Create an m-file that will read-out the data for you. Figure 2.20 shows you a simple MATLAB script that will do the job. The data is stored in a variable and can be easily saved.

Table 2.3: NI-DAQ USB-6211 Overview

Property	Description
Availability	Meetshop (Jos van Driel)
Read-out	MATLAB/Labview
Sampling frequency $f_s$	250kSa/s (max)
Resolution	16-bit
Voltage-range	-10V to 10V
Accuracy	2.69mV
Sensitivity	91.6 $\mu$ V
Analog input channels	8 (Diff.), 16 (Sin.)

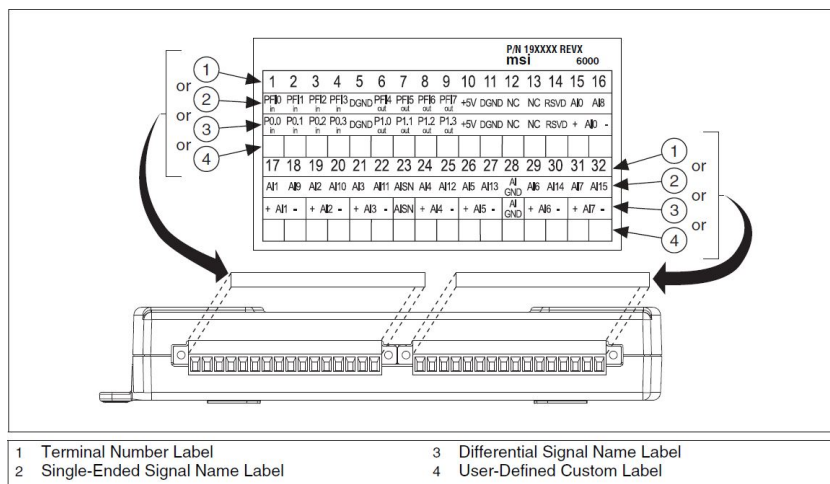


Figure 2.19: Overview of the USB-6211 available ports.

```

%% NI DataAcquisition
s = daq.createSession('ni'); %Create a NI session
s.DurationInSeconds = 1; %Measurement time (seconds)
s.Rate = 250e3; %Sample frequency (Sa/s)
ch = addAnalogInputChannel(s, 'Dev2', 'ai0', 'Voltage'); %Differential measurement
% ch.InputType = 'SingleEnded'; %Single-ended
voltage = startForeground(s); %Acquire data and store in variable data

```

Figure 2.20: Simple MATLAB script for data-acquisition.

## PHASE-LOCKING TWO AGILENT 33220A DIGITAL FUNCTION GENERATORS

Two phase-locked waveforms can be easily generated by two digital function generators. In this research, the Agilent 33220A function generators were used. This document will quickly guide you through the process on how to setup these generators.

- 1) Determine the frequency and mutual phase difference between the respective waveforms you would like to create. E.g. if you want to create a sine and cosine waveform, the mutual phase difference is 90 degrees.
- 2) Setup the two function generators, where one serves as the master while the other serves as the slave. Connect the 'Sync' output connector of the master to the 'External trigger' input connector of the slave. This 'External' trigger is located at the back of the function generator.
- 3) On the master you should enable the 'Sync on' setting in the 'Utility' section. Do not forget to do this, otherwise the procedure will not work.
- 4) Now you should enable the 'Burst' mode on the slave function generator. The figure below shows you where this button is located. Please determine the amount of cycles depending on your signal frequency, just try some settings that work for your frequency. In the trigger setup tab, within the 'Burst' mode, you can define where the slave should trigger. In the same 'Burst' mode you can set the mutual phase difference between the two waveforms.

The figures below show an overview of the two function generators and their connections, moreover a photograph of the scope is added where a 100kHz sine and cosine signal are phase locked.



Figure 2.21: Photograph of the master and slave function generator and their output connections

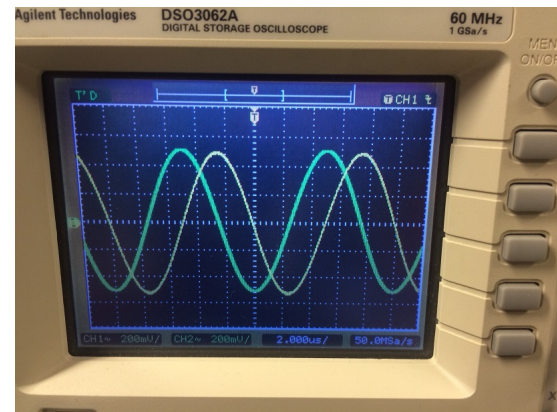


Figure 2.22: Photograph of scope's display for a 100kHz phase-locked sine and cosine signal



